

# Mindboggling morphometry of human brains

Arno Klein<sup>1\*</sup>, Satrajit S. Ghosh<sup>2,3</sup>, Forrest S. Bao<sup>4</sup>, Joachim Giard<sup>5,#a</sup>, Yrjö Häme<sup>6,#b</sup>, Eliezer Stavsky<sup>6,#c</sup>,  
Noah Lee<sup>6,#d</sup>, Brian Rossa<sup>7,#e</sup>, Martin Reuter<sup>8</sup>, Elias Chaibub Neto<sup>9</sup>, Anisha Keshavan<sup>10</sup>

<sup>1</sup> Child Mind Institute, New York, NY, USA

<sup>2</sup> McGovern Institute for Brain Research, Massachusetts Institute of Technology, Cambridge, MA, USA

<sup>3</sup> Department of Otolaryngology, Harvard Medical School, Boston, MA, USA

<sup>4</sup> Department of Electrical and Computer Engineering, University of Akron, Akron, OH, USA

<sup>5</sup> University of Louvain, Belgium

<sup>6</sup> Columbia University, NY, NY, USA

<sup>7</sup> TankThink Labs, Boston, MA, USA

<sup>8</sup> Harvard Medical School, Cambridge, MA, USA

<sup>9</sup> Sage Bionetworks, Seattle, WA, USA

<sup>10</sup> University of California San Francisco, San Francisco, CA, USA

<sup>#a</sup>Current Address: Axinesis, Wavre, Belgium

<sup>#b</sup>Current Address: Comptel, Helsinki, Finland

<sup>#c</sup>Current Address: Blend Labs, Inc., San Francisco, CA, USA

<sup>#d</sup>Current Address: 1010data, New York, NY, USA

<sup>#e</sup>Current Address: FØCAL, Cambridge, MA, USA

\* Corresponding author

E-mail: [arno@binarybottle.com](mailto:arno@binarybottle.com) (AK1)

## Abstract

Mindboggle (<http://mindboggle.info>) is an open source brain morphometry platform that takes in

26 preprocessed T1-weighted MRI data and outputs volume, surface, and tabular data containing label,  
27 feature, and shape information for further analysis. In this article, we document the software and  
28 demonstrate its use in studies of shape variation in healthy and diseased humans. The number of  
29 different shape measures and the size of the populations make this the largest and most detailed shape  
30 analysis of human brains ever conducted. Brain image morphometry shows great potential for  
31 providing much-needed biological markers for diagnosing, tracking, and predicting progression of  
32 mental health disorders. Very few software algorithms provide more than measures of volume and  
33 cortical thickness, and more subtle shape measures may provide more sensitive and specific biomarkers.  
34 Mindboggle computes a variety of (primarily surface-based) shapes: area, volume, thickness, curvature,  
35 depth, Laplace-Beltrami spectra, Zernike moments, etc. We evaluate Mindboggle's algorithms using the  
36 largest set of manually labeled, publicly available brain images in the world and compare them against  
37 state-of-the-art algorithms where they exist. All data, code, and results of these evaluations are publicly  
38 available.

39

#### 40 **Author Summary**

41 Brains vary in many ways, including their shape. Analysing differences in shape between brains  
42 or changes in brain shape over time has been used to characterize morphology of diseased  
43 brains, but these analyses conventionally rely on simple volumetric shape measures. We  
44 believe that access to a greater variety of shape measures could provide greater sensitivity and  
45 specificity to morphological disturbances, and could aid in diagnosis, tracking, and prediction  
46 of the progression of mental health disorders. Mindboggle is open source software that  
47 provides neuroscientists (and indeed, anyone interested in computing shapes) tools for  
48 computing a variety of shape measures, including area, volume, thickness, curvature, geodesic  
49 depth, travel depth, Laplace-Beltrami spectra, and Zernike moments. In addition to  
50 algorithmic contributions, we conducted evaluations and applied Mindboggle to conduct the

51 most detailed shape analysis of human brains.

52

## 53 **1. Introduction**

54 This article summarizes years of work on the Mindboggle project (<http://mindboggle.info>), including  
55 development and application of software that automates the extraction, identification, and shape analysis  
56 of features from human brain magnetic resonance imaging (MRI) data. The principal original  
57 contributions of the Mindboggle software include (1) a hybrid approach to combine different software  
58 packages' gray/white matter segmentations, (2) new algorithms for volume and surface shape measures  
59 devoted to brain images, including travel depth and cortical thickness, and (3) new shape-based feature  
60 extraction algorithms for brain structures such as folds, sulci, and fundi. Further contributions described  
61 in this article include (1) evaluations of Mindboggle volume and surface shape measurement algorithms  
62 against other software algorithms, (2) evaluation of Mindboggle's fundus extraction algorithm against  
63 other software algorithms, (3) Python implementations of algorithms for general-purpose shape  
64 measures such as Laplace-Beltrami spectra and Zernike moments, and (4) application of Mindboggle to  
65 provide the most detailed shape measures computed on human brain image data. This Introduction  
66 provides background and motivation for the project, Methods outlines the history of the project and the  
67 software's input, processing steps, and output, Results describes evaluations and applications of the  
68 software, and Discussion provides commentary and future directions.

69

### 70 **1.1. The promise of brain imaging for finding biological markers of mental illness**

71 Brain images have been used to derive biological markers of mental illness and disease for years, most  
72 notably to predict prognoses among patients with behavioral disorders, often more accurately than  
73 current behavioral instruments such as widely used scales and structured interviews. For example, brain  
74 images have been used to predict relapse in methamphetamine dependence [1], □ onset of psychosis in  
75 at-risk individuals [2,3], □ recovery from depression eight months later [4], □ response to drug treatment

76 for depression [5,6], anxiety [7]□, and for cognitive behavioral therapy in schizophrenia [8] and social  
77 anxiety disorder [9,10] (see [11] for a more extensive review).□ Despite the above promising  
78 experimental results, there is still a dearth of reliable biomarkers [12].□ The importance of identifying  
79 new biomarkers is reflected in the National Institute of Mental Health’s Strategic Objectives: “Currently,  
80 very few biomarkers have been identified for mental disorders due in part to their complexity and an  
81 incomplete understanding of the neurobiological basis of mental disorders...”

82

### 83 **1.2. Variation in human brains and the “correspondence problem”**

84 A significant impediment to our understanding of mental health is variation in human brain anatomy,  
85 physiology, function, connectivity, response to treatment, and so on. The normal range of variation must  
86 first be established to determine what is outside of this range, and only then can we hope to address  
87 neuropsychiatric assessment, diagnosis, prognosis, treatment, or prevention. An effective biomarker  
88 traditionally consists of one or more measures that maximize the separability between groups while  
89 minimizing the variance within each group. Brain images provide many ways of measuring different  
90 aspects of the brain, but it is not always clear how to compare these measures over time or across  
91 individuals. Comparing brains presumes that a brain-to-brain correspondence or mapping has been  
92 solved. To do this, scientists ubiquitously co-register images to each other, either individually or in  
93 groups, commonly with the use of a standard template brain or labeled atlas. However, registration alone  
94 does not guarantee correspondence [13] and templates are often not representative of the group being  
95 studied [14,15].□ Additional factors that affect the quality of registration are often ignored. For  
96 example, we have empirically demonstrated that registration algorithms vary widely in their accuracy  
97 [16], that even the best require removal of non-brain matter to perform adequately [17,18],□ and  
98 conventional registration is less robust to missing regions than feature-based registration methods [19].□  
99 Despite this, many brain imaging studies co-register brains based on image similarity, assume alignment  
100 of corresponding anatomy [20], and compare the brains at the level of a small extent such as a sphere or

101 rectilinear volume, which can be on the order of 1/100,000th the volume of the image.

102

### 103 **1.3. Anatomical feature-based correspondence**

104 Neuroanatomists rely instead on high-level “features” such as distinctive cortical folding patterns and  
105 relative positions of subcortical structures to consistently identify anatomical structures or label brain  
106 regions ([21,22]; survey results related to [23]; personal communications with neuroanatomists). Such  
107 morphological features may also be identified by using multimodal imaging data and classifiers trained  
108 on such data [24]. In addition to whole (gyrus and sulcus) folds, components such as sulcal pits and  
109 sulcal fundi hold promise for establishing correspondence across brains. Sulcal pits, points of maximal  
110 depth or curvature in sulci, are interesting because they may be well conserved structures formed early  
111 in development [25–27] and have been used to characterize conditions such as polymicrogyria [28]. □  
112 Sulcal fundi are defined as curves that run along the depths of sulci. They form branching skeletons that  
113 simplify the complex pattern of folds of the brain, may be measured for morphometry studies, and are  
114 used to help define the boundaries between gyri [22]. Like pits, fundi are thought to characterize early  
115 stages of morphological development, and therefore may exhibit abnormalities in neurodevelopmental  
116 and heritable disorders.

117

### 118 **1.4. Shape measures as biomarkers**

119 To compare features across individuals we need to quantify them. One quantification method is to  
120 characterize the quantities and distributions of grayscale values within a volume, but this does not work  
121 well for features of limited extent, such as a point, line, or surface patch. Another method is to coregister  
122 a given brain or brain feature with a reference and to define similarity with the reference based on the  
123 registration itself (deformation-based morphometry). Yet another method is to directly measure shape,  
124 where shape is defined as the geometrical information that remains when location, scale and rotation are  
125 removed from an object [29]. Publicly available brain image datasets that include any shape measures

126 usually provide only a few shape measures per anatomical region: volume (such as the Internet Brain  
127 Volume Database, <http://www.nitrc.org/projects/ibvd>), surface area, and/or cortical thickness. These  
128 measures are useful for studies of neurogenesis or atrophy in morphological development, degeneration,  
129 injury, and disease progression. Volume measurement is almost ubiquitous in such studies, and cortical  
130 thickness measures derived from structural MRI data have been reported to help characterize a variety of  
131 disorders [30] such as mild cognitive impairment and Alzheimer’s disease [31–33], multiple sclerosis  
132 [34], schizophrenia [35], autism spectrum disorder [36], and alcohol dependence [37], and to predict  
133 onset or progression of, for example, Alzheimer’s disease [38–44], major depressive disorder [45], and  
134 attention-deficit/hyperactivity disorder [46].

135

136 More subtle shape measures may provide more sensitive and specific biomarkers, and combining shape  
137 measures in a multivariate analysis can improve results over any single measure [47]. The lack of shape  
138 measures may be attributable to the paucity of software programs such as BrainVisa [48,49]  
139 ([https://www.nitrc.org/projects/brainvisa\\_ext](https://www.nitrc.org/projects/brainvisa_ext)) that compute more nuanced measures. □ Sulcal width has  
140 been used to differentiate between groups with mild cognitive impairment [50] and global and local  
141 gyrification indices computed from sulci have been used to characterize schizophrenia [51] and early-  
142 onset vs. intermediate-onset bipolar disorder as well as bipolar and unipolar depression [52–54]. More  
143 abstract shape measures such as Zernike moments (see below) have been used in patient classification,  
144 such as to distinguish cases of dementia [55].

145

## 146 **2. Methods**

147 Mindboggle (<http://mindboggle.info>) is an open source brain morphometry platform that takes in  
148 preprocessed T1-weighted MRI data, and outputs volume, surface, and tabular data containing label,  
149 feature, and shape information for further analysis. Mindboggle can be run on the command line as  
150 “mindboggle” and also exists as a cross-platform Docker container for convenience and

151 reproducibility of results. The software runs on Linux and is written in Python 3 and Python-wrapped  
152 C++ code called within a modular Nipype pipeline framework (<http://nipy.org/nipype>, doi:  
153 10.5281/zenodo.50186) to promote a modular, flexible design that captures provenance information  
154 [56]. We have tested the software most extensively with Python 3.5.1 on Ubuntu Linux 14.04. Issues  
155 and bugs are tracked on GitHub (<https://github.com/nipy/mindboggle/issues>) and support questions are  
156 posted on NeuroStars (<https://neurostars.org/t/mindboggle/>) with the tag “*mindboggle*”.

157

158 Mindboggle’s flexible, modular, open source pipeline facilitates the addition of functions for computing  
159 almost any shape measure in any programming language. We initialized Mindboggle with shape  
160 measures that we thought have great potential for describing the shapes of brain structures and that  
161 complement shape measures supplied by existing software packages. It is just as easy to include  
162 functions in Mindboggle for volume-based as it is for surface-based measures, but we decided to focus  
163 primarily on surface-based shape measures to complement the volume-based methods available in  
164 standard brain image analysis packages. We also want to emphasize in this work intrinsic shape  
165 measures of brain structures rather than shapes inferred by registration-based methods such as voxel-  
166 based, tensor-based, and deformation-based morphometry that rely on a reference or canonical template  
167 and are sensitive to errors in registration. We also do not consider density values to be intrinsic shape  
168 measures, as they do not describe the shape of an object, but quantify values obtained within an object,  
169 in an analogous manner as one would quantify an fMRI signal or PET ligand binding within a voxel or  
170 region of interest.

171  
172  
173

## 174 **2.1. History of the Mindboggle open source brain morphometry platform**

175 **2005:** The initial version of the Mindboggle software (<https://osf.io/gfwn/>) was written in Matlab  
176 (Mathworks, Inc., Natick, MA) as part of a doctoral dissertation [57]. It introduced a feature-driven

177 approach to label human brain MRI data using one atlas [19] or multiple atlases [58].

178

179 **2009:** With generous funding from the National Institute of Mental Health, we began to write

180 Mindboggle from scratch in Python with some surface mesh measurements programmed in C++, all run

181 from a software pipeline written in the Nipype framework.

182

183 **2010:** To ensure that the most consistent and accurate anatomical labels are assigned to brain image

184 data, we introduced a new cortical labeling protocol with 62 labels (**Fig 1**) called the Desikan-Killiany-

185 Tourville (DKT) protocol [22,23] (<http://mindboggle.info/labels.html>). We applied this protocol to

186 manually edit the anatomical labels for 101 individuals (20 of which also include CMA non-cortical

187 labels [59] (<http://www.cma.mgh.harvard.edu/manuals/segmentation/>)). The resulting Mindboggle-101

188 dataset [22,60] (<http://mindboggle.info/data.html>, <https://osf.io/nhtur/>) is still the largest publicly

189 available set of manually edited human brain labels in the world. These brains were used to construct

190 multiple templates [61] and atlases [62], including the joint fusion [63] volume atlas

191 (<https://osf.io/d2cmy/?action=download&version=1>) used by the Mindboggle software for volume-

192 based segmentation and labeling, and the DKT-40 and DKT-100 surface atlases [62] used for labeling

193 cortical surfaces by the FreeSurfer software package [64–66]

194 (<https://surfer.nmr.mgh.harvard.edu/fswiki>). The DKT-100 is used as the default atlas for labeling brains

195 in FreeSurfer (version 6). The Mindboggle-101 brains are used for evaluations and shape analyses

196 described in the Results section.

197

198 **2013:** A prototype for online, interactive visualization of Mindboggle shape analysis data won a

199 hackathon challenge at the Human Brain Mapping (HBM 2013) conference. After use of the XTK

200 (<https://github.com/xtk/X#readme>) WebGL JavaScript library [67,68], we used the threejs

201 (<http://threejs.org/>) and D3 JavaScript libraries in a second (HBM 2015 [69]) and third (HBM 2016)

202 hackathon to create the ROYGBIV online interactive brain image viewer (**Fig 1**;

203 <http://roygbiv.mindboggle.info>), which is under active development

204 (<https://github.com/binarybottle/roygbiv>).

205

206 **Fig 1. Cortical labels displayed in the ROYGBIV interactive online brain image viewer.**

207 The anatomical labels included in the DKT cortical labeling protocol [22] used to label the Mindboggle-  
208 101 data are displayed on a left cortical surface. These two panels show the current state of our  
209 prototype for a browser-based interactive visualization of the left hemisphere of a human brain [69] and  
210 accompanying plot of some of Mindboggle's shape measures for a selected region  
211 (<http://roygbiv.mindboggle.info>).

212

213 **2015:** Mindboggle processed Alzheimer's Disease Neuroimaging Initiative (ADNI; [adni.loni.usc.edu](http://adni.loni.usc.edu);  
214 [70]) and AddNeuroMed [71] data for an international Alzheimer's disease challenge [72]  
215 (<https://www.synapse.org/Synapse:syn2290704/wiki/60828>). Teams performed statistical analyses on  
216 Mindboggle shape measures to try and determine which brains had Alzheimer's disease, mild cognitive  
217 impairment, or were healthy, and to try and estimate a cognitive measure (mini-mental state exam  
218 score). The Results section presents an analysis of some of these data.

219

220 **2016:** Mindboggle is launched for broader public use after making the following improvements:

- 221 ● Software ported from Python 2 to Python 3
- 222 ● Docstring tests provided for almost every function
- 223 ● GitHub repository transferred to the nipy.org community's GitHub account
- 224 ● Online documentation updated automatically
- 225 ● Online support via NeuroStars with the tag "*mindboggle*"
- 226 ● Online tests run automatically

227

228 The documentation is updated online (<https://readthedocs.org/projects/mindboggle>) and the tests are  
229 updated online (<https://circleci.com/gh/nipy/mindboggle>) every time a commit is made to the GitHub  
230 repository (<https://github.com/nipy/mindboggle>).

231

## 232 **2.2. Input data and preprocessing**

233 For running individual functions on surface meshes, the only inputs to the software are outer cortical

234 surface meshes constructed from T1-weighted MRI data by software such as FreeSurfer, Caret [73] or  
235 BrainVISA [48], once converted to an appropriate format (see below). For this study we used FreeSurfer  
236 v5.1-derived labels and meshes, but the recently released FreeSurfer version 6 is recommended because  
237 it uses Mindboggle's DKT-100 surface-based atlas (with the DKT31 labeling protocol) by default to  
238 generate labels on the cortical surfaces, and generates corresponding labeled cortical and non-cortical  
239 volumes (wmparc.mgz) [74]. To preprocess data for use by Mindboggle, run the following FreeSurfer  
240 command on a T1-weighted `$IMAGE` file (e.g., `subject1.nii.gz`) to output a `$SUBJECT` folder (e.g.,  
241 `subject1`):

242

```
243 recon-all -all -i $IMAGE -s $SUBJECT
```

244

245 The `recon-all` command performs many steps (<https://surfer.nmr.mgh.harvard.edu/fswiki/recon-all>),  
246 but the ones that are most relevant include (1) segmentation of the brain image into different tissue  
247 classes (gray/white/cerebrospinal fluid), (2) reconstruction of a triangular surface mesh approximating  
248 the pial surface for each brain hemisphere, and (3) anatomical labeling of each surface and each volume.

249

250 To refine segmentation, labeling, and volume shape analysis, Mindboggle optionally takes output from  
251 the Advanced Normalization Tools (ANTs, v2.1.0rc3 or higher recommended;

252 <http://stnava.github.io/ANTs/>), which performs various image processing steps such as brain volume

253 extraction [17,75], tissue-class segmentation [76], and registration-based labeling [16,18,75]. To

254 generate the ANTs transforms and segmentation files used by Mindboggle, run the

255 `antsCorticalThickness.sh` script [75] on the same `$IMAGE` file, set an output `$PREFIX`, and

256 provide paths to the OASIS-30 Atropos template files in directory `$TEMPLATE` (backslash denotes a

257 line return):

258

```
259 antsCorticalThickness.sh -d 3 -a IMAGE -o PREFIX \  
260     -e $TEMPLATE/T_template0.nii.gz \  
261     -t $TEMPLATE/T_template0_BrainCerebellum.nii.gz \  
262     -m $TEMPLATE/T_template0_BrainCerebellumProbabilityMask.nii.gz \  
263     -f $TEMPLATE/T_template0_BrainCerebellumExtractionMask.nii.gz \  
264     -p $TEMPLATE/Priors2/priors%d.nii.gz
```

265

266 Links to the template (<https://osf.io/bx35m/?action=download&version=1>) and example input data  
267 (<https://osf.io/8cf5z/>) can be found on the Mindboggle website.

268

### 269 **2.3. Mindboggle processing steps**

270 The following steps are performed by Mindboggle (<http://mindboggle.info/software.html>):

271 1: Convert FreeSurfer formats to NIfTI volumes and VTK surfaces.

272 2: Optionally combine FreeSurfer and ANTs gray/white segmented volumes and fill with labels.

273 3: Compute volumetric shape measures for each labeled region.

274 4: Compute shape measures for every cortical surface mesh vertex.

275 5: Extract cortical surface features.

276 6: Segment cortical surface features with labels.

277 7: Compute shape measures for each cortical surface label or sulcus.

278 8: Compute statistics for each shape measure in Step 4 for collections of vertices.

279

#### 280 **Step 1: Convert FreeSurfer formats to NIfTI volumes and VTK surfaces:**

281 Mindboggle performs all of its processing in two open standard formats: NIfTI (.nii.gz;

282 <http://nifti.nimh.nih.gov/>) for volume images and VTK (.vtk, Visualization Toolkit; <http://www.vtk.org/>)

283 for surface meshes. ANTs output already supports NIfTI; given FreeSurfer input, the first step that

284 Mindboggle performs is to convert FreeSurfer volume and surface formats to NIfTI and VTK for further  
285 processing. All volume images in this study have a resolution of  $1 \times 1 \times 1 \text{ mm}^3$  per voxel (volume  
286 element). All surface-based shape measures are computed on the “pial surface” (cortical-cerebrospinal  
287 fluid boundary) by default, since it is sensitive to differences in cortical thickness.

288

289 **Step 2: Optionally combine FreeSurfer and ANTs gray/white segmented volumes and fill with**  
290 **labels:**

291 This optional step of the pipeline will be skipped in the future when methods for tissue class  
292 segmentation of T1-weighted MR brain images into gray and white matter improve. FreeSurfer and  
293 ANTs make different kinds of mistakes while performing tissue class segmentation (**Fig 2**). After visual  
294 inspection of the gray/white matter boundaries in over 100 EMBARC  
295 (<http://embarc.utsouthwestern.edu/>, <https://clinicaltrials.gov/ct2/show/NCT01407094>) brain images  
296 processed by FreeSurfer, we found that at least 25 brains had significant overcropping of the brain,  
297 particularly in ventral regions such as lateral and medial orbitofrontal cortex and inferior temporal lobe  
298 due to poor surface mesh reconstruction in those regions. This corroborates Klauschen’s observation that  
299 FreeSurfer underestimates gray matter and overestimates white matter [77]. We also found that ANTs  
300 tends to include more cortical gray matter than FreeSurfer, but at the expense of losing white matter that  
301 extends deep into gyral folds, and sometimes includes non-brain tissue such as transverse sinus, sigmoid  
302 sinus, superior sagittal sinus, and bony orbit.

303

304 Mindboggle attempts to reconcile the differences between FreeSurfer and ANTs segmentations by  
305 combining them. The `relabel_volume` function converts the (`wmparc.mgz`) labeled file generated  
306 by FreeSurfer and the (`BrainSegmentation.nii.gz`) segmented file generated by the ANTs `Atropos`  
307 function [76] to binary files of pseudo-white matter and gray (including deep gray) matter. The  
308 `combine_2labels_in_2volumes` function overlays FreeSurfer white matter atop ANTs cortical

309 gray, by taking the union of cortex voxels from both binary files as gray matter, the union of the non-  
310 cortex voxels from the two binary files as white matter, and assigning intersecting cortex and non-cortex  
311 voxels as non-cortex. While this strategy often preserves gray matter bordering the outside of the brain,  
312 it still suffers from over-inclusion of non-brain matter, and sometimes replaces true gray matter with  
313 white matter in areas where surface reconstruction makes mistakes.

314  
315 The FreeSurfer/ANTs hybrid segmentation introduces new gray-white matter boundaries, so the  
316 corresponding anatomical (gyral-sulcal) boundaries generated by FreeSurfer and ANTs need to be  
317 updated accordingly. Mindboggle uses ImageMath's `PropagateLabelsThroughMask` function  
318 in ANTs to propagate both FreeSurfer and ANTs anatomical labels to fill the gray and white matter  
319 volumes independently. The FreeSurfer-labeled cerebellum voxels overwrite any intersecting cortex  
320 voxels, in case of overlap.

321

322 **Fig 2. FreeSurfer and ANTs gray/white matter segmentation.**

323 Left: Coronal slice of a T1-weighted brain MRI. Middle: Cross-section of FreeSurfer inner (magenta)  
324 and outer (green) cortical surfaces overlaid on top of the same slice. The red ellipse circumscribes a  
325 region where the FreeSurfer surface reconstruction failed to include gray matter on the periphery of the  
326 brain. Right: Cross-section of ANTs segmentation. The blue ellipse circumscribes a region where the  
327 ANTs segmentation failed to segment white matter within a gyrus that the FreeSurfer correctly  
328 segmented (compare with the middle panel). The purple box in the lower right highlights a region  
329 outside of the brain that the ANTs segmentation mistakenly includes as gray matter. To reconcile some  
330 of these discrepancies, Mindboggle currently includes an optional processing step that combines the  
331 segmentations from FreeSurfer and ANTs. This step essentially overlays the white matter volume  
332 enclosed by the magenta surface in the middle panel atop the gray/white segmented volume in the right  
333 panel.

334

335 **Step 3: Compute volumetric shape measures for each labeled region:**

- 336
- volume
  - thickness of cortical labels (`thickinthehead`)
- 337

338 As mentioned in the Introduction, the most common shape measures computed for brain image data are  
339 volume and cortical thickness for a given labeled region of the brain. Volume measurements are

340 influenced by various factors such as cortical thickness, surface area [78], and microstructural tissue  
341 properties [79]. Computing the volume per labeled region is straightforward: Mindboggle's  
342 `volume_per_brain_region` function simply multiplies the volume per voxel by the number of  
343 voxels per region. In contrast, cortical thickness can be estimated using a variety of MRI processing  
344 algorithms [49,75,80–83]. Since Mindboggle accepts FreeSurfer data as input, we include FreeSurfer  
345 cortical thickness [80] estimates with Mindboggle's shape measures. When surface reconstruction from  
346 MRI data produces favorable results (see above), FreeSurfer cortical thickness measures can be highly  
347 reliable [81,84,85]. See Results for our evaluation of cortical thickness measures.

348

349 To avoid surface reconstruction-based problems with the cortical thickness measure, we built a function  
350 called `thickinthehead` that computes a simple thickness measure for each cortical region from a  
351 brain image volume without relying on surface data (**Fig 3**). The `thickinthehead` function first  
352 saves a brain volume that has been segmented into cortex and non-cortex voxels into separate binary  
353 files, then resamples these cortex and non-cortex files from, for example,  $1\text{mm}^3$  to  $0.5\text{mm}^3$  voxel  
354 dimensions to better represent the contours of the cortex. Next it extracts outer and inner boundary  
355 voxels of the cortex by morphologically eroding the cortex by one (resampled) voxel bordering the  
356 outside of the brain and bordering the inside of the brain (non-cortex). Then it estimates the middle  
357 cortical surface area by the average volume of the outer and inner boundary voxels of the cortex.  
358 Finally, it estimates the thickness of a labeled cortical region as the volume of the labeled region divided  
359 by the middle surface area of that region. The `thickinthehead` function calls the `ImageMath`,  
360 `Threshold`, and `ResampleImageBySpacing` functions in ANTs.

361

362 **Fig 3. Thickinthehead estimates average cortical thickness per brain region.**

363 Mindboggle's `thickinthehead` algorithm estimates cortical thickness for each brain region without  
364 relying on cortical surface meshes by dividing the volume of a region by an estimate of its middle  
365 surface area. Clockwise from lower left: 3-D cross-section and sagittal, coronal, and axial slices. The  
366 colors represent the inner and outer "surfaces" of cortex created by eroding gray matter bordering white  
367 matter and eroding gray matter bordering the outside of the brain. The middle surface area is estimated

368 by taking the average volume of these inner and outer surfaces.

369

370 **Step 4: Compute shape measures for every cortical surface mesh vertex:**

371 ● surface area

372 ● mean curvature

373 ● geodesic depth

374 ● travel depth

375 ● convexity (FreeSurfer)

376 ● thickness (FreeSurfer)

377

378 Aside from the convexity and thickness measures inherited from FreeSurfer, shape measures computed  
379 for each vertex of a cortical surface triangular mesh are generated by Mindboggle's open source C++  
380 code (using the Visualization Toolkit, VTK) developed by Joachim Giard: surface area, mean curvature,  
381 geodesic depth, and travel depth. Surface area is computed per vertex (as opposed to per face of the  
382 mesh to be consistent with all other Mindboggle shape measures) as the area of the Voronoi polygon  
383 enclosing the vertex (**Fig 4**). Area can be used to normalize other values computed within a given  
384 region such as a gyrus or sulcus [86].

385

386 **Fig 4. Surface area per vertex.**

387 Mindboggle computes surface area for each surface mesh vertex as the area of the Voronoi polygon  
388 enclosing the vertex. Left: Lateral view of a left cortical hemisphere colored by surface area per vertex.  
389 Right: Closeup of the surface mesh. Mindboggle uses area to normalize other shape values computed  
390 within a given region such as a gyrus or sulcus.

391

392 Curvature is an obvious shape measure for a curved and folded surface like the cerebral cortex and has  
393 the potential to help make inferences about other characteristics of the brain, such as sulcus width,  
394 atrophy [87,88], structural connections [89] and differential expansion of the cortex [90]. Mindboggle  
395 computes both mean and Gaussian curvatures based on the relative direction of the normal vectors in a

396 small neighborhood (**Fig 5**), which works best for low resolution or for local peaks, but can be sensitive  
397 to the local linear geometry of the mesh. Increasing the radius of the neighborhood mitigates this  
398 sensitivity, so a neighborhood parameter corresponding to the radius of a geodesic disk is defined in the  
399 unit of the mesh. If coordinates are in millimeters, the default setting of 2 results in an analysis of the  
400 normal vectors within a 2mm radius disk. Other options include computing both mean and Gaussian  
401 curvatures based on the local ratios between a filtered surface and the original surface area (the filtering  
402 is done using Euclidean distances, so it's best for less accurate but fast visualization), or computing the  
403 mean curvature based on the direction of the displacement vectors during a Laplacian filtering (a good  
404 approximation based on the Laplacian, but underestimates very large, negative or positive, curvatures  
405 due to saturation).

406

407 **Fig 5. Curvature per vertex.**

408 Mindboggle computes curvature for each surface mesh vertex. This medial view of the left cortical  
409 hemisphere is colored by curvature per vertex (green indicates flat regions).

410

411 Depth is an important measure characterizing the highly folded surface of the human cerebral cortex.  
412 Since much of the surface is buried deep within these folds, an accurate measure of depth is useful for  
413 defining and extracting deep features, such as sulci [91,92], sulcal fundus curves [93–95], and sulcal pits  
414 [26,96,97]. Depth may also serve as an indicator of developmental stage [26].

415

416 We are aware of three predominant methods for measuring depth of points on the surface of the cerebral  
417 cortex, where depth is the distance between a given point on the brain surface to an outer reference  
418 surface of zero depth (the portions of the brain surface in contact with the outer reference surface are  
419 gyral crowns or crests). The first is Euclidean depth, the distance along a straight path from the point on  
420 the brain to the outer reference surface. A straight path has the undesirable property that it will cross  
421 through anything, which can make a highly folded surface indistinguishable from a slightly folded  
422 surface that fills the same volume. The second is geodesic depth, the shortest distance along the surface

423 of the brain from the point to where the brain surface makes contact with the outer reference surface.  
424 Geodesic paths are very sensitive to slight or gradual changes in depth, resulting in exaggerated  
425 distances where the outer reference surface does not wrap the brain closely. Geodesic paths are also  
426 greatly affected by cavities, so distances can be exaggerated where there are irregularities, particularly in  
427 the bottoms of sulcus folds. The third measure, FreeSurfer software's "convexity," while not explicitly  
428 referred to as depth, is used to indicate relative depth. It is based on the displacement of surface mesh  
429 vertices after inflating the surface mesh [64]. This can result in assigning positive depth to points on the  
430 outermost surface of the brain such as on a gyral crest, however, which is not consistent with an intuitive  
431 measure of depth.

432

433 Travel depth was introduced as a hybrid depth measure for macromolecules, defined as the shortest  
434 distance that a solvent molecule would travel from the convex hull of the macromolecule without  
435 penetrating the macromolecule surface. It was first defined for surfaces but using a voxel-based  
436 algorithm [98] that uses Dijkstra's algorithm for finding shortest paths, and was later refined to use a  
437 much faster and more accurate vertex-based computation [99]. A detailed description of the latter  
438 follows. The travel depth algorithm constructs a combination of Euclidean paths outside the cortical  
439 surface and estimated geodesic paths along the cortical surface. The principal idea of the algorithm lies  
440 in the classification of a surface into "visible" and "hidden" areas (**Fig 1 in Supplement 1**). A point on  
441 the surface is considered "visible" by another point if they can be connected by a straight line without  
442 intersecting the volume enclosed by the surface. In other words, there is a "line of sight" between the  
443 two points that does not run through the interior of the surface. A point is considered "hidden" from  
444 another point if it is not visible and can only be reached by a path running either along the surface or  
445 connecting points of the surface without intersecting the enclosed volume.

446

447 The above implementations of travel depth use a convex hull (**Fig 2 in Supplement 1**), as do most

448 measures of cortical depth such as the adaptive distance transform [100], while other algorithms do not  
449 define a zero-depth reference surface but rely instead on convergence of an algorithm, such as the depth  
450 potential map [101]. The shape of the brain is concave in places, resulting in some gyral crowns that do  
451 not touch the convex hull. For example, in **Fig 3 in Supplement 1**, the gyri of the medial temporal lobe  
452 are assigned positive depth, resulting in an unreasonably high depth for the folds of that region. Since  
453 the convex hull is not suitable for application to brain images, or for surfaces with global concavities, we  
454 define and construct a different reference surface that we call the wrapper surface (**Fig 5 in Supplement**  
455 **1**). The wrapper surface has to be chosen such that the top of a gyrus has zero depth. We compute a  
456 wrapper surface as follows. We create a volume image representing the interior of the mesh, dilate this  
457 image with a probe of radius  $r$ , then erode it with the same probe. This operation is also known as  
458 morphological closing, and it is important to carefully set the probe radius. If the radius is too large, the  
459 wrapper surface will be similar to the convex hull, and if the radius is too small, the wrapper surface will  
460 be too close to the original surface and the travel depth will be close to zero even inside folds. We used  
461 an empirically determined radius of 5 mm. The wrapper surface mesh is an isosurface of this  
462 morphologically closed image volume, created using the marching cubes algorithm. On a brain mesh  
463 with 150,000 vertices and 300,000 triangles, the algorithm takes around 200 seconds on an ordinary  
464 computer when the wrapper surface is provided. The generation of the wrapper surface takes an  
465 additional 20 seconds for a probe radius of 5 mm.

466

467 Mindboggle's travel depth algorithm assigns a depth value to every vertex in a mesh, is faster and more  
468 accurate than voxel-based approaches, assigns more reasonable path distances that are less sensitive to  
469 surface irregularities and imaging artifacts than geodesic distances, and is faithful to the topology of the  
470 surface. **Fig 6** shows an example of geodesic and travel depth values, and the Results section  
471 summarizes our comparison of travel depth with geodesic depth and FreeSurfer convexity measures.

472

473 **Fig 6. Geodesic depth and travel depth per vertex.**

474 Mindboggle computes geodesic depth (left) and travel depth (right) for each surface mesh vertex. This  
475 medial view of the sulcus folds from the left cortical hemisphere is colored by depth, with the deepest  
476 vertices in yellow. Note that the deepest vertices according to geodesic depth reside toward the center of  
477 the insula (center fold), whereas the deepest vertices according travel depth run along the deepest  
478 furrows of the insula, as one would expect.  
479

480 **Step 5: Extract cortical surface features:**

- 481 ● folds
- 482 ● fundus per fold

483

484 Mindboggle extracts hierarchical structures from cortical surfaces [102,103], including folds and fundus  
485 curves running along the depths of the folds. A fold is a group of connected, deep vertices (left side of  
486 **Fig 7**). When assigned anatomical labels, folds can be broken up into sulci (right side of **Fig 7**). To  
487 extract folds, a depth threshold is used to segment deep vertices of the surface mesh. We have observed  
488 in the histograms of travel depth measures of cortical surfaces that there is a rapidly decreasing  
489 distribution of low depth values (corresponding to the outer surface, or gyral crowns) with a long tail of  
490 higher depth values (corresponding to the folds). Mindboggle's `find_depth_threshold` function  
491 therefore computes a histogram of travel depth measures, smooths the histogram's bin values, convolves  
492 to compute slopes, and finds the depth value for the first bin with zero slope. The `extract_folds`  
493 function uses this depth value, segments deep vertices, and removes extremely small folds (empirically  
494 set at 50 vertices or fewer out of a total mesh size of over 100,000 vertices).

495

496 **Fig 7. Cortical fold extraction and sulcus segmentation.**

497 Top left: Lateral view of the left hemisphere of a brain with folds labeled red. Mindboggle extracts  
498 cortical surface folds based on a depth threshold that it computes from the distribution of travel depth  
499 values. Bottom left: individually colored folds from the same brain. The red surface shows that folds can  
500 be broadly connected, depending on the depth threshold, and therefore do not map one-to-one to  
501 anatomical region labels. Top right: The same folds with individually colored anatomical labels. These  
502 labels can be automatically or manually assigned (as in the case of this Mindboggle-101 subject).  
503 Bottom right: Individually colored sulci. Mindboggle uses the anatomical labels to segment folds into  
504 sulci, defined as folded portions of cortex whose opposing banks are labeled with sulcus label pairs in  
505 the DKT labeling protocol [22]. Each label pair is unique to one sulcus and represents a boundary

506 between two adjacent gyri, so sulcus labels are useful to establish correspondences across brains.  
507 Portions of folds that are missing are not defined as sulci by the DKT labeling protocol.  
508

509 A fundus is a branching curve that runs along the deepest and most highly curved portions of a fold (**Fig**  
510 **8**). As mentioned above, fundi can serve as boundaries between anatomical regions and are interesting  
511 for their relationship to morphological development and disorders. But they are too tedious, time-  
512 consuming, and difficult to be drawn in a consistent manner on the surface meshes derived from MR  
513 images. Mindboggle provides multiple functions for extracting fundi which are optionally generated  
514 from the command line; the `extract_fundi` function described below is used by default and is  
515 evaluated against other fundus extraction methods in the Results section. This function extracts one  
516 fundus from each fold by finding the deepest vertices inside the fold, finding endpoints along the edge of  
517 the fold, connecting the former to the latter with tracks that run along deep and curved paths (through  
518 vertices with high values of travel depth multiplied by curvature), and running a final filtration step. A  
519 more detailed description of these four steps follows. In the first step, the deepest vertices are those with  
520 values at least two median absolute deviations above the median (non-zero) value. If two of these deep  
521 vertices are within (a default of) 10 edges from each other, the vertex with the higher value is chosen to  
522 reduce the number of possible fundus paths as well as to reduce computation time. To find the endpoints  
523 in the second step, the `find_outer_endpoints` function propagates multiple tracks from seed  
524 vertices at median depth in the fold through concentric rings toward the fold's edge, selecting maximal  
525 values within each ring, and terminating at candidate endpoints. The final endpoints are those candidates  
526 at the end of tracks that have a high median value. If two candidate endpoints are within (a default of) 10  
527 edges from each other, the endpoint with the higher value is chosen; otherwise the resulting fundi can  
528 have spurious branching at the fold's edge. The `connect_points_erosion` function connects the  
529 deepest fold vertices to the endpoints with a skeleton of 1-vertex-thick curves by erosion. It erodes by  
530 iteratively removing simple topological points and endpoints in order of lowest to highest values, where

531 a simple topological point is a vertex that when added to or removed from an object on a surface mesh  
532 (such as a fundus curve) does not alter the object's topology.

533

534 **Fig 8. Sulcal fundi.**

535 This figure shows three views of the outside of a single sulcus (taken from the top middle fold in **Fig 7**)  
536 to clearly show a simple example of a fundus (red branching curve). Mindboggle extracts one fundus  
537 from each fold by finding the deepest vertices inside the fold, finding endpoints along the edge of the  
538 fold, connecting the former to the latter with tracks that run along deep and curved paths, and running a  
539 final filtration step. Just as anatomical labels segment folds into sulci, sulcus labels segment fold fundi  
540 into sulcal fundi.

541

542 **Step 6: Segment cortical surface features with labels:**

- 543 ● sulci from folds
- 544 ● fundus per sulcus

545

546 Since folds are defined as deep, connected areas of a surface, and since folds may be connected to each  
547 other in ways that differ across brains, there usually does not exist a one-to-one mapping between folds  
548 of one brain and those of another. To address the correspondence problem, we need to find just those  
549 portions of the folds that correspond across brains. To accomplish this, Mindboggle segments folds into  
550 sulci, which do have a one-to-one correspondence across non-pathological brains (right side of **Fig 7**).  
551 Mindboggle defines a sulcus as a folded portion of cortex whose opposing banks are labeled with one or  
552 more sulcus label pairs in the DKT labeling protocol. Each label pair is unique to one sulcus and  
553 represents a boundary between two adjacent gyri, and each vertex has one gyrus label. The  
554 `extract_sulci` function assigns vertices in a fold to a sulcus in one of two cases. In the first case, if  
555 a vertex has a label that is in only one label pair in the fold, it is assigned that label pair's sulcus if it can  
556 be connected through vertices with one of the pair's labels to the boundary between the two labels. In  
557 the second case, the `segment_regions` function propagates labels from a label boundary to vertices  
558 whose labels are in multiple label pairs in the fold. Once sulci are defined, the `segment_by_region`

559 function uses sulcus labels to segment fold fundi into sulcal fundi, which, like sulci, are features with  
560 one-to-one correspondence across non-pathological brains.

561

562 **Step 7: Compute shape measures for each cortical surface label or sulcus:**

- 563 ● surface area
- 564 ● Laplace-Beltrami spectrum
- 565 ● Zernike moments

566

567 In addition to shape measures computed for each vertex of a surface (Step 4), Mindboggle also  
568 computes shape measures that apply to collections of vertices such as gyri and sulci (Step 6): surface  
569 area (sum of surface areas across vertices), Laplace-Beltrami spectra, and Zernike moments.

570

571 Martin Reuter established important properties of the spectrum that relates to a shape's intrinsic  
572 geometry with his "Shape-DNA" method [104–106]. This approach is specifically valuable for non-rigid  
573 shapes, such as anatomical structures: it is insensitive to local bending, as it quantifies only non-  
574 isometric deformation, e.g., stretching. The spectrum corresponds to the frequencies of the modes of the  
575 shape and its real-valued components, the eigenvalues, therefore describe different levels of detail (from  
576 more global low-frequency features to localized high-frequency details, **Fig 9**). The eigen-  
577 decomposition of the Laplace-Beltrami operator is computed via a finite element method (FEM).

578 Mindboggle's Python `fem_laplacian` function is based on Reuter's Shape-DNA Matlab  
579 implementation, and their eigenvalues agree to the 16th decimal place, attributable to machine precision.

580

581 To calculate the distance between the descriptors of two shapes, Reuter describes several approaches,  
582 e.g.,  $L^p$ -norm, Hausdorff distance and weighted distances. One of the more prominent and simple  
583 distance measures is the Euclidean distance ( $L_2$  norm) of the first  $N$  smallest (non-zero) eigenvalues,

584 where  $N$  is called the truncation parameter. To account for the linearly increasing magnitude of the  
585 eigenvalues (Weyl's law), Reuter recommends to divide each value by its area and its index (done by  
586 default in Mindboggle). As an alternative, the Weighted Spectral Distance (WESD) [107] is included in  
587 Mindboggle (but not used by default). It computes the  $L^p$ -norm of a weighted difference between the  
588 vectors of the  $N$  smallest Eigenvalues. This approach forms a pseudo-metric and also avoids domination  
589 of higher components on the final distance, making it insensitive to the truncation parameter  $N$  (with a  
590 decreasing influence as  $N$  gets larger). Additionally, the choice of  $p$  (for the  $L^p$ -norm) influences how  
591 sensitive the metric is to finer as opposed to coarser differences in the shape; as  $p$  increases, WESD  
592 becomes less sensitive to differences at finer scales.

593

594 **Fig 9. Laplace-Beltrami spectra.**

595 Mindboggle computes a Laplace-Beltrami spectrum for each feature (gyrus, sulcus, etc.), which relates  
596 to its intrinsic geometry, after Reuter et al.'s "Shape-DNA" method [104–106]. The components of the  
597 spectrum correspond roughly to the level of detail of the shape, from global to local, shown left to right  
598 for the 2nd, 3rd, and 9th spectral components for two different left brain hemispheres (top and bottom).  
599

600 Moments can describe the shape of objects, images, or statistical distributions of points, and different  
601 types of moments confer different advantages [108]. Geometric moments of 3-D coordinates have been  
602 used to construct shape descriptors for human brain morphometry [109] because of desirable  
603 characteristics such as invariance to rotation, symmetry, and scale, and they can be computed for any  
604 topology. Zernike moments [110] have also been applied to human brain morphometry for classifying  
605 dementia patients [55] and confer several advantages over geometric moments. They form a set of  
606 orthogonal descriptors, where each descriptor contains independent information about the structure,  
607 allowing the original shape to be reconstructed from the moments. They have been extensively  
608 characterized for shape retrieval performance and are robust to noise. Zernike moments can also be  
609 calculated at different orders (levels of detail): low order moments represent low frequency information  
610 while high orders represent high frequency information. Mikhno et al. [55] implemented Pozo et al.'s

611 [111] efficient 3-D implementation of Zernike moments in Matlab, and helped us test our Python  
612 implementation to ensure they give consistent results. The length of the descriptors exponentially  
613 increases with order, so order 20 yields 121 descriptors while order 35 yields 342, for example. Values  
614 are generally less than or equal to one, with values much greater than one indicating instability in the  
615 calculation, which could be due to the way the mesh is created or due to calculating at an order that is  
616 too high given the resolution or size of the object.

617

618 **Step 8: Compute statistics for each shape measure in Step 4 for collections of vertices:**

- 619 ● median
- 620 ● median absolute deviation
- 621 ● mean
- 622 ● standard deviation
- 623 ● skewness
- 624 ● kurtosis
- 625 ● lower quartile
- 626 ● upper quartile

627

628 There can be thousands of vertices in a single feature such as a gyrus, sulcus, or fundus, so it makes  
629 sense to characterize a feature's shape as either a distribution of per-vertex shape values (Step 4), or as a  
630 single shape value (Step 7). Mindboggle's `stats_per_label` function generates tables containing  
631 both, with summary statistical measures representing the distributions of per-vertex shape values.

#### 632 **2.4. Mindboggle output**

633 Example output data generated by Mindboggle is accessible at <http://osf.io/8cf5z/>. As with the input  
634 formats, volume files are in NIFTI format, surface meshes are in VTK format, and tables are comma-  
635 delimited. Each file contains integers that correspond to anatomical labels or features (0-24 for sulci).

636 All output data are in the original subject's space, except for additional surfaces and mean coordinates in  
637 MNI152 space [112]. The **Appendix** contains a directory tree with outputs from most of the optional  
638 arguments, and does not include interim results stored in a working directory or downloaded files in a  
639 cache directory.

640

### 641 **3. Results**

642 Mindboggle has been and continues to be subjected to a variety of evaluations (<https://osf.io/x3up7/>) and  
643 applied in a variety of contexts. In this section, we compare related shape measures (**3.1**), evaluate  
644 fundus extraction algorithms (**3.2**), and evaluate the consistency of shape measures between scans (**3.3**).  
645 We also demonstrate Mindboggle's utility in measuring shape differences between left and right  
646 hemispheres (**3.4**), and in measuring brain shape variation (**3.5**).

647

#### 648 **3.1. Comparisons between brain shape measures**

649 We compared shape measures with one another in a representative individual from the Mindboggle-101  
650 data set (**Fig 10**) and for the entire data set (**Fig 11**, **Fig 12**, and **Fig 13**) to emphasize to the reader that  
651 shape measures are not independent of one another and that care must be taken when comparing  
652 differently defined shape measures or when using one as a proxy for another. **Fig 10** plots over 130,000  
653 vertices of one brain hemisphere, where the coordinates are two different shape measures assigned to  
654 each vertex: geodesic depth by travel depth (top) and mean curvature by travel depth (bottom). This  
655 figure demonstrates that curvature is positively correlated with depth and that geodesic depth produces  
656 higher shape values than travel depth, and may exaggerate depth, such as in the insula (also clearly  
657 evident in **Fig 6** and **Fig 11**).

658

#### 659 **Fig 10. Relationships between brain shape measures.**

660 In these plots, we compare a pair of shape measures for each vertex of each right cortical region in a  
661 representative individual from the Mindboggle-101 brains, colored arbitrarily by region.

662 Top: In this plot comparing two measures of depth, geodesic depth is higher than travel depth, and may

663 exaggerate depth, such as in the insula (gray dots extending to the upper left).  
664 Bottom: In this plot of mean curvature by travel depth, we again see that the shape measures are not  
665 independent of one another. As one might expect, we see greater curvature at greater depth.  
666

667 **Fig 11. Comparison between cortical depth measures.**

668 This superposition of two box and whisker plots is a comparison between two measures of cortical  
669 surface depth applied to the 101 Mindboggle-101 brains: Mindboggle's travel depth and geodesic depth.  
670 These surface measures are computed for every mesh vertex, so the plots were constructed from median  
671 depth values, with one value per labeled region. Geodesic depth deviates most from travel depth for the  
672 insular regions (far right).  
673

674 **Fig 12. Comparison between cortical curvature measures.**

675 This superposition of two box and whisker plots is a comparison between two measures of cortical  
676 surface curvature applied to the 101 Mindboggle-101 brains: Mindboggle's mean curvature and  
677 FreeSurfer's curvature measure. These surface measures are computed for every mesh vertex, so the  
678 plots were constructed from median curvature values, with one value per labeled region. Deviations  
679 between the two curvature values are most evident for the entorhinal regions (fourth pair from the left).  
680

681 **Fig 13. Comparison between cortical thickness measures.**

682 This superposition of two box and whisker plots is a comparison between two measures of cortical  
683 thickness applied to the 101 Mindboggle-101 brains: Mindboggle's *thickinthehead* (black) and  
684 FreeSurfer's thickness (red) measures. FreeSurfer's thickness is defined per surface mesh vertex, so the  
685 red plot was constructed from median thickness values, with one value per labeled region.  
686  
687

688 While it may be useful to compare the distributions of two different shape measures for each region over  
689 a population (as in **Fig 11**, **Fig 12**, and **Fig 13**), we also computed the distance correlation between  
690 related shape measures for each cortical region in the Mindboggle-101 subjects (**Table 1**;  
691 <https://osf.io/9cn7s/>). To compare related (travel and geodesic depth, mean and FreeSurfer curvature)  
692 surface shape measures, we computed the distance correlation between each pair of shape measures  
693 across all of the vertices per region, and computed the average of the distance correlations per region  
694 across the 101 subjects. Distance correlation enabled a comparison of the pattern of values for a given  
695 region between two shape measures without regard for their absolute values. Mindboggle's travel depth  
696 and geodesic depth measures were very highly correlated for 60 of the 62 regions, with distance  
697 correlations ranging from 0.91 to 1.00 (all but four greater than 0.95). The two outliers were the left and  
698 right insula (0.29 and 0.31), which corroborates our earlier assertion that geodesic depth can exaggerate  
699 depth values compared to travel depth in regions such as the insula. Mindboggle's mean curvature and

700 FreeSurfer's curvature measures had distance correlations ranging from 0.73 (insula) to 0.91 (rostral  
701 middle frontal), with the top 10 values all for frontal and parietal regions. Since *thickinthehead*  
702 values are computed per region, not per vertex, to compare *thickinthehead* with median FreeSurfer  
703 thickness values, we constructed a pair of vectors for each region with 101 values, each value  
704 corresponding to the shape measure for that region in a subject, and computed the distance correlation  
705 between the two vectors. The highest distance correlations (0.8 to 0.7) were obtained by frontal and  
706 parietal regions, and the lowest correlations (0.3 to 0.2) by precuneus, parahippocampal, fusiform, and  
707 cingulate regions.

708

709

710

711

712

Cortical region	travel depth vs. geodesic depth		mean curvature vs. FreeSurfer curvature		thickinthehead vs. FreeSurfer thickness	
	left	right	left	right	left	right
caudal anterior cingulate	0.97	0.96	0.83	0.83	0.39	0.38
caudal middle frontal	0.99	0.99	0.88	0.88	0.72	0.70
cuneus	0.99	0.99	0.84	0.83	0.52	0.51
entorhinal	0.96	0.96	0.77	0.75	0.38	0.33
fusiform	0.97	0.97	0.83	0.83	0.22	0.20
inferior parietal	0.99	0.99	0.88	0.88	0.56	0.50
inferior temporal	0.98	0.98	0.84	0.84	0.31	0.39
isthmus cingulate	0.91	0.93	0.78	0.79	0.19	0.30
lateral occipital	0.99	0.99	0.86	0.86	0.54	0.57
lateral orbitofrontal	0.92	0.92	0.80	0.81	0.54	0.54
lingual	0.97	0.98	0.83	0.82	0.45	0.62
medial orbitofrontal	0.97	0.97	0.82	0.82	0.42	0.57
middle temporal	0.99	1.00	0.88	0.88	0.49	0.40
parahippocampal	0.96	0.97	0.81	0.84	0.44	0.26
paracentral	0.99	0.99	0.87	0.87	0.64	0.59
pars opercularis	0.98	0.98	0.89	0.89	0.65	0.47
pars orbitalis	0.98	0.98	0.90	0.90	0.43	0.50
pars triangularis	1.00	1.00	0.90	0.90	0.63	0.47
pericalcarine	0.96	0.97	0.76	0.78	0.34	0.37
postcentral	1.00	1.00	0.87	0.87	0.71	0.63
posterior cingulate	0.99	0.99	0.84	0.83	0.29	0.38
precentral	0.99	0.99	0.88	0.88	0.70	0.54
precuneus	0.98	0.98	0.86	0.86	0.29	0.48
rostral anterior cingulate	0.98	0.97	0.80	0.79	0.26	0.35
rostral middle frontal	0.99	0.99	0.91	0.91	0.75	0.61
superior frontal	0.99	0.99	0.89	0.89	0.80	0.71
superior parietal	0.99	0.99	0.89	0.89	0.69	0.76
superior temporal	0.99	0.99	0.86	0.85	0.59	0.52
supramarginal	1.00	1.00	0.88	0.87	0.65	0.60
transverse temporal	0.97	0.98	0.76	0.74	0.67	0.69
insula	0.29	0.31	0.73	0.73	0.46	0.38

713

714 **Table 1. Distance correlations between related shape measures**

715 To compare pairs of related (travel and geodesic depth, mean and FreeSurfer curvature) surface shape  
716 measures, we computed the distance correlation between vectors of shape values for all vertices in each  
717 cortical region, and averaged the distance correlations across the 101 Mindboggle-101 subjects. For  
718 *thickinthehead* and FreeSurfer thickness measures, we computed the distance correlation between  
719 vectors of median shape values for all 101 Mindboggle-101 subjects for each cortical region.  
720

721

722 **3.1.1. Comparison between travel depth and FreeSurfer's convexity measure**

723 As described above, travel depth uses a reference wrapper surface that lies closer to the cortical surface  
724 than a convex hull would. In particular, the wrapper lies closer to the medial temporal lobe, so the gyri  
725 in this area have depth values equal to zero as one would want. FreeSurfer's convexity measure [80],  
726 often used to indicate relative depth, leads to non-zero and even negative values for vertices on these  
727 gyri (**Fig 4 in Supplement 1**). We computed the mean and standard deviation of four statistical  
728 measures of travel depth and FreeSurfer's convexity values for over 130,000 vertices in a representative  
729 cortical surface. For this comparison, we consider a point to be close to the wrapper surface if the  
730 distance between the two is smaller than 0.1 mm, a depth value is considered small if it is less than 0.1  
731 mm, and a convexity value is considered small if it is less than the smallest convexity value for all the  
732 vertices in the mesh. For travel depth, by definition all vertices (and only those vertices) that are close to  
733 the wrapper surface have a small depth. For convexity, almost all vertices (97.71%) that have a small  
734 convexity value are close to the wrapper surface, but they represent only 6.89% of the vertices close to  
735 the wrapper surface (**Table 1 in Supplement 1**). One conclusion we drew from this comparison is that  
736 while both travel depth and FreeSurfer's convexity measures represent depth well for deep portions of a  
737 surface, travel depth provides a more faithful representation for shallow portions.

738

739 **3.1.2. Comparison between cortical thickness measures**

740 We are aware of only one study directly comparing FreeSurfer with manual cortical thickness measures,  
741 where the manual estimates were made in nine gyral crowns of a post-mortem brain, selected for their

742 low curvature and high probability of having been sampled perpendicular to the plane of section [113].  
743 We compared `thickinthehead`, FreeSurfer, and ANTs cortical thickness estimates in different  
744 populations, including the Mindboggle-101 subjects (**Fig 13**) and in the 40 EMBARC control subjects  
745 (<https://osf.io/jwhea/>). For 16 cortical regions in the 40 subjects, we measured scan-rescan reliability of  
746 cortical thickness measures, and we compared thickness measures with published estimates based on  
747 manual delineations of MR images of living brains [114]. Forty percent of FreeSurfer estimates for the  
748 640 labels were in the published ranges of values, whereas almost ninety percent of  
749 `thickinthehead`'s estimates were within these ranges (as mentioned above, Klauschen observed  
750 that FreeSurfer underestimates gray matter and overestimates white matter [77]). ANTs values deviated  
751 further from the published estimates and were less reliable (greater inter-scan and inter-subject ranges)  
752 than the FreeSurfer or `thickinthehead` values.

753

### 754 **3.2. Evaluation of fundus extraction algorithms**

755 This section presents the first quantitative comparison of fundus extraction software algorithms. Since  
756 there exists no ground truth for fundus curves, we must resort to other means of evaluation. We leave it  
757 to future work to determine their utility for practical applications such as diagnosis and prediction of  
758 disorders. Since the DKT labeling protocol defines many of its anatomical label boundaries along  
759 approximations of fundus curves, we used the manually edited anatomical label boundaries in the  
760 Mindboggle-101 dataset as gold standard data to evaluate the positions of fundi extracted by four  
761 different algorithms in 2013. Specifically, for each of the 48 fundi/sulci defined by the DKT protocol,  
762 we computed the mean of the minimum Euclidean distances from the label boundary vertices in the  
763 sulcus to the fundus vertices in the sulcus, as well as from the fundus vertices in the sulcus to the label  
764 boundary vertices in the sulcus. The algorithms included Mindboggle's default  
765 `connect_points_erosion` function described above, Forrest Bao's pruned minimum spanning  
766 tree algorithm [102], Gang Li's algorithm [115], and an algorithm in the BrainVisa software [95]. The

767 final algorithm was omitted from the results because too few fundi were extracted to make an adequate  
768 comparison (BrainVisa extracts 65 sulci per hemisphere, and it is possible that the program did not  
769 define some folds as sulci that contain fundi according to the DKT labeling protocol).

770

771 All of the fundi, summary statistics, and results are available online (<https://osf.io/r95wb/>). While there  
772 was no clear winner, we can summarize our comparison by computing the mean distance between fundi  
773 and label boundaries across all sulci for the three methods and by tallying how many sulci had the  
774 smallest mean distance among the methods. When measured from label boundaries to fundi, Gang Li's  
775 and Mindboggle's fundi were closer than were Forrest Bao's (mean distances of 2.09mm and 2.38mm  
776 vs. 3.65mm, respectively; 25 and 21 vs. 2 closest sulci), whereas when measured from fundi to label  
777 boundaries, Forrest Bao's fundi were closer than were Mindboggle's or Gang Li's (mean distances of  
778 3.33mm vs. 4.06mm and 4.65mm, respectively; 41 vs. 5 and 2 closest sulci). When measuring from  
779 either direction, the maximum distances averaged across all sulci were higher for Forrest Bao's fundi  
780 (11.65mm and 11.61mm) than for Mindboggle's (10.84mm and 9.75mm) or Gang Li's (11.12mm and  
781 6.87mm).

782

### 783 **3.3. Consistency of shape measures between MRI scans of the same person**

784 For a shape measure to be useful in comparative morphometry, it should be more sensitive to differences  
785 in anatomy than to differences in MRI scanning setup or artifacts. To get a sense of the degree of  
786 scan/rescan consistency of our shape measures, we ran Mindboggle on 41 Mindboggle-101 subjects with  
787 a second MRI scan (OASIS-TRT-20 and MMRR-21 cohorts). We computed the fractional shape  
788 difference per cortical region as the absolute value of the difference between the region's shape values  
789 for the two scans divided by the first scan's shape value. For the volumetric shape measures (volume  
790 and `thickinthehead` cortical thickness), shape value is computed by region; for the surface-based  
791 shape measures (area, travel and geodesic depth, mean and FreeSurfer curvature, and FreeSurfer

792 thickness), shape value is assigned the median value across all vertices within a region. All shape tables,  
793 statistical summary tables, and accompanying plots are available online (<https://osf.io/mhc37/>).

794

795 **Table 2a** gives the average across the 41 subjects of the fractional shape differences between MRI scans  
796 for each of the 31 left cortical regions, and for each shape measure, and **Table 2b** gives a statistical  
797 summary of the differences. In general, the values are low enough to suggest high inter-scan shape  
798 consistency, but we will point out values greater than or equal to 0.10. Of the volumetric shape measures  
799 (volume and *thickinthehead*), only one value exceeded or equaled 0.10: entorhinal volume (0.21).  
800 Entorhinal cortex had the second smallest volume of manually labeled MRI cortical regions in 101  
801 healthy human brains [22] (after transverse temporal cortex; see <https://osf.io/st7nk/>), and low  
802 scan/rescan consistency for small brain structures corroborates Jovicich’s observation in 2013 [116]:  
803 “We found that the smaller structures (pallidum and amygdala) yielded the highest absolute volume  
804 reproducibility errors, approximately 3.8% (average across sites), whereas all other structures had errors  
805 in the range 1.8-2.2% (average across sites), with the longitudinal segmentation analysis. Our absolute  
806 % errors in test-retest volumetric estimates are comparable to those reported by previous studies  
807 (Kruggel et al., 2010; Morey et al., 2010; Reuter et al., 2012).” Regarding cortical thickness measures,  
808 Jovicich observed: “The thickness reproducibility results of the various structures were largely  
809 consistent across sites and vendors, with errors in the range 0.8 – 5.0% for the longitudinal analysis  
810 (table 7).” Of the surface shape measures, the following exceeded or equaled 0.10 for three measures  
811 (travel depth, geodesic depth, and FreeSurfer curvature): entorhinal, medial orbitofrontal, and (caudal  
812 anterior, rostral anterior, and isthmus) cingulate regions; and for at least one of the measures: lateral  
813 orbitofrontal, parahippocampal, pericalcarine, and insular regions. The greatest differences were for  
814 FreeSurfer curvature in the pericalcarine (0.34), insula (0.28), and rostral anterior cingulate (0.23),  
815 followed by entorhinal volume (0.21) and travel depth (0.20). FreeSurfer curvature had the greatest  
816 number of outliers (**Table 2b**) and was the only shape measure that spanned negative to positive values,

817 so regions with very small median curvature values could have inflated these fractions. Future  
818 evaluations will assess the impact that differences in scans have on morphometry-based clinical  
819 research.

820

821

822

823

<b>Cortical region</b>	<b>volume</b>	<b>thick</b>	<b>area</b>	<b>travel</b>	<b>geodesic</b>	<b>curv</b>	<b>FScurv</b>	<b>FSthick</b>
caudal anterior cingulate	0.04	0.05	0.05	0.10	0.10	0.06	0.18	0.04
caudal middle frontal	0.04	0.05	0.05	0.03	0.03	0.05	0.07	0.04
cuneus	0.04	0.06	0.04	0.06	0.05	0.03	0.05	0.05
entorhinal	0.21	0.06	0.09	0.20	0.16	0.06	0.14	0.05
fusiform	0.03	0.04	0.03	0.04	0.05	0.03	0.05	0.03
inferior parietal	0.03	0.04	0.02	0.03	0.02	0.04	0.05	0.04
inferior temporal	0.05	0.04	0.03	0.07	0.06	0.03	0.06	0.02
isthmus cingulate	0.04	0.08	0.07	0.11	0.13	0.04	0.11	0.04
lateral occipital	0.03	0.02	0.03	0.08	0.07	0.03	0.04	0.04
lateral orbitofrontal	0.09	0.05	0.04	0.08	0.10	0.05	0.09	0.04
lingual	0.03	0.04	0.04	0.05	0.06	0.03	0.04	0.04
medial orbitofrontal	0.07	0.06	0.06	0.14	0.10	0.06	0.11	0.05
middle temporal	0.03	0.05	0.03	0.04	0.03	0.03	0.05	0.03
parahippocampal	0.04	0.04	0.04	0.11	0.12	0.06	0.09	0.03
paracentral	0.07	0.04	0.05	0.08	0.08	0.04	0.07	0.06
pars opercularis	0.04	0.06	0.04	0.03	0.03	0.03	0.06	0.03
pars orbitalis	0.06	0.05	0.04	0.06	0.07	0.05	0.09	0.04
pars triangularis	0.03	0.06	0.03	0.06	0.05	0.04	0.09	0.04
pericalcarine	0.06	0.06	0.04	0.03	0.03	0.10	0.34	0.07
postcentral	0.04	0.02	0.03	0.03	0.03	0.03	0.05	0.06
posterior cingulate	0.04	0.08	0.05	0.09	0.09	0.05	0.09	0.04
precentral	0.04	0.03	0.02	0.02	0.02	0.03	0.04	0.04
precuneus	0.03	0.05	0.03	0.03	0.04	0.03	0.07	0.04
rostral anterior cingulate	0.04	0.09	0.06	0.10	0.10	0.08	0.23	0.05
rostral middle frontal	0.04	0.07	0.03	0.04	0.03	0.05	0.06	0.04
superior frontal	0.02	0.04	0.02	0.06	0.04	0.03	0.04	0.03
superior parietal	0.04	0.03	0.02	0.03	0.03	0.04	0.05	0.05
superior temporal	0.04	0.05	0.03	0.02	0.03	0.02	0.04	0.02
supramarginal	0.04	0.04	0.03	0.04	0.04	0.04	0.07	0.04
transverse temporal	0.06	0.07	0.04	0.02	0.03	0.04	0.07	0.06
insula	0.03	0.09	0.03	0.01	0.01	0.05	0.28	0.03

824

825 **Table 2a. Shape differences between MRI scans**

826 This table lists shape differences between two scans of the same brain averaged across 41 brains. The  
 827 shape differences are computed for each of the 31 left cortical regions as the absolute value of the  
 828 difference between the region’s shape values between the two scans divided by the first scan’s shape  
 829 value. For the surface-based shape values, we used the median value for all vertices within each region.  
 830 [thick = *thickinthehead* cortical thickness; travel = travel depth; geodesic = geodesic depth; curv =  
 831 mean curvature; FScurv = FreeSurfer’s curvature; FSthick = FreeSurfer’s thickness]

832

833

834

	mean	std	min	25%	50%	75%	max	>0.50	>0.25
volume	0.047	0.044	0.002	0.019	0.035	0.063	0.213	5	21
<i>thickinthehead</i>	0.052	0.046	0.001	0.017	0.039	0.078	0.183	0	16
area	0.039	0.038	0.001	0.014	0.030	0.054	0.182	2	6
travel depth	0.061	0.050	0.002	0.024	0.050	0.085	0.229	1	36
geodesic depth	0.059	0.049	0.002	0.022	0.048	0.082	0.222	2	35
mean curvatures	0.044	0.038	0.001	0.016	0.033	0.059	0.170	0	7
FreeSurfer curvature	0.094	0.091	0.004	0.033	0.070	0.127	0.433	17	78
FreeSurfer thickness	0.041	0.036	0.001	0.014	0.032	0.060	0.147	0	0

835

836 **Table 2b. Summary statistics of shape differences between MRI scans**

837 This table gives a statistical summary of the shape differences between two scans of the same brain for  
 838 41 brains. The “mean” column is the average of the mean values in **Table 1a**, while the other columns  
 839 contain averages of their respective values over the 31 regions; for example, the “std” column contains  
 840 the average of the std values computed for each of the 31 regions. [>0.50 and >0.25 give the number of  
 841 regions (out of 1,271 = 31 regions times 41 subjects) where the fractional absolute difference was above  
 842 0.50 and 0.25, respectively.]

843

844

845

846

847

### 848 **3.4. Measuring shape differences between left and right hemispheres**

849 To measure interhemispheric shapes differences, we computed the fractional shape difference per  
850 cortical region as in the preceding section, replacing inter-scan differences with interhemispheric  
851 differences (<https://osf.io/dp4zy/>), and using all 101 Mindboggle-101 brains. **Table 3a** gives the average  
852 across the 101 subjects of the fractional shape differences between hemispheres for each of the 31  
853 cortical regions, and for each shape measure, and **Table 3b** gives a statistical summary of the  
854 differences. The values are much higher than the corresponding inter-scan differences in the previous  
855 section, suggesting that shape differences between hemispheres are greater than shape differences  
856 between MRI scans of the same hemisphere.

857

858

859

860  
861

Cortical regions	volume	thick	area	travel	geodesic	curv	FScurv	FSthick
caudal anterior cingulate	0.26	0.06	0.32	0.27	0.21	0.11	0.32	0.06
caudal middle frontal	0.14	0.04	0.20	0.14	0.13	0.10	0.16	inf
cuneus	0.12	0.06	0.17	0.32	0.24	0.10	0.15	0.04
entorhinal	0.17	0.08	0.23	0.41	0.30	0.10	0.21	0.09
fusiform	0.08	0.05	0.15	0.14	0.13	0.07	0.10	0.04
inferior parietal	0.23	0.05	0.25	0.11	0.11	0.06	0.09	0.03
inferior temporal	0.09	0.04	0.14	0.21	0.16	0.07	0.08	0.05
isthmus cingulate	0.14	0.04	0.17	0.21	0.20	0.10	0.18	0.07
lateral occipital	0.09	0.04	0.14	0.22	0.18	0.05	0.07	0.04
lateral orbitofrontal	0.06	0.05	0.11	0.23	0.26	0.09	0.12	0.05
lingual	0.11	0.04	0.12	0.15	0.13	0.08	0.11	0.05
medial orbitofrontal	0.08	0.05	0.18	0.27	0.19	0.10	0.17	0.06
middle temporal	0.11	0.04	0.12	0.17	0.15	0.07	0.10	0.05
parahippocampal	0.11	0.05	0.13	0.36	0.29	0.15	0.19	0.08
paracentral	0.16	0.04	0.18	0.25	0.20	0.08	0.16	0.04
pars opercularis	0.18	0.04	0.33	0.20	0.23	0.10	0.17	0.05
pars orbitalis	0.22	0.05	0.32	0.37	0.40	0.13	0.20	0.06
pars triangularis	0.20	0.05	0.32	0.30	0.24	0.12	0.21	0.06
pericalcarine	0.18	0.06	0.21	0.10	0.11	0.45	inf	0.06
postcentral	0.09	0.03	0.12	0.13	0.13	0.10	0.14	0.05
posterior cingulate	0.13	0.04	0.13	0.21	0.18	0.09	0.15	0.05
precentral	0.07	0.03	0.09	0.10	0.10	0.07	0.11	0.04
precuneus	0.06	0.03	0.11	0.17	0.14	0.07	0.13	0.03
rostral anterior cingulate	0.22	0.07	0.36	0.21	0.18	0.10	1.23	0.06
rostral middle frontal	0.08	0.03	0.17	0.14	0.12	0.08	0.09	0.04
superior frontal	0.06	0.03	0.14	0.19	0.14	0.06	0.07	0.04
superior parietal	0.07	0.02	0.15	0.12	0.12	0.07	0.12	0.03
superior temporal	0.07	0.03	0.12	0.10	0.10	0.09	0.11	0.04
supramarginal	0.12	0.03	0.19	0.17	0.16	0.08	0.13	0.04
transverse temporal	0.24	0.06	0.24	0.10	0.10	0.18	0.27	0.06
insula	0.06	0.04	0.07	0.05	0.03	0.10	0.32	0.05

862  
863  
864  
865  
866  
867  
868  
869

**Table 3a. Shape differences between left and right hemispheres**

Shape differences between hemispheres are computed for each of the 31 cortical regions in all 101 of the Mindboggle-101 subjects as the absolute value of the difference between the region's left and right shape values divided by the left shape value. For the surface-based shape values, we used the median value for all vertices within each region. (Refer to **Table 1a** caption for abbreviations.)

870

	mean	std	min	25%	50%	75%	max	>0.50	>0.25
volume	0.129	0.091	0.002	0.058	0.117	0.180	0.448	38	443
thickinthehead	0.044	0.036	0.001	0.017	0.037	0.064	0.169	0	4
area	0.183	0.163	0.002	0.074	0.148	0.248	1.025	165	744
travel depth	0.198	0.199	0.003	0.074	0.150	0.257	1.251	211	764
geodesic depth	0.173	0.163	0.002	0.067	0.133	0.229	1.009	148	658
mean curvatures	0.104	0.113	0.002	0.038	0.079	0.141	0.872	59	192
FreeSurfer curvature	0.190	0.435	0.003	0.074	0.150	0.250	3.890	205	626
FreeSurfer thickness	0.050	0.077	0.001	0.018	0.036	0.062	0.691	23	28

871

872

873 **Table 3b. Summary statistics of shape differences between left and right hemispheres**

874 This table gives a statistical summary of the interhemispheric shape differences for the 101 Mindboggle-  
 875 101 brains. The “mean” column is the average of the mean values in **Table 3a**, while the other columns  
 876 contain averages of their respective values over the 31 regions; for example, the “std” column contains  
 877 the average of the std values computed for each of the 31 regions. [ $>0.50$  and  $>0.25$  give the number of  
 878 regions (out of  $3,131 = 31$  regions times 101 subjects) where the fractional absolute difference was  
 879 above 0.50 and 0.25, respectively.]

880

881

882 **3.7. Measuring human brain shape variation**

883 To estimate the normal range of variation in the shapes of healthy adult human brains, we applied  
 884 Mindboggle software in 2015 to compute shape measures for our Mindboggle-101 dataset (see **2.1**: 2010  
 885 above). The result is the largest set of shape measures computed on healthy human brain data (See  
 886 **Supplement 2** and <https://osf.io/gzshf/> for detailed results) [117,118]. We are treating these as  
 887 normative data against which anyone can compare similarly processed images of different healthy  
 888 populations as well as patient populations.

889

890 The data we analysed consist of repeated measurements on five distinct real-valued shape measures  
 891 (mean curvature, geodesic depth, travel depth, FreeSurfer convexity, and FreeSurfer thickness) for each  
 892 of 31 distinct regions per brain hemisphere in each of the 101 subjects. Each subject was scanned at one

893 of five different laboratories. At the bottom of **Fig 14** is one example of the many heatmap tables we  
894 have generated from these data (all results are accessible at <https://osf.io/d7hx8/>). Each table presents  
895 one value for each labeled region or sulcus for each of the 101 subjects. The value is either volume or  
896 `thickinthehead` cortical thickness for volumetric images, or for one of the five surface shape  
897 measures above, one of eight summary statistical measures (mean, median, median absolute deviation,  
898 standard deviation, lower and upper quartiles, skewness, and kurtosis) computed across all vertices in  
899 the surface mesh of the labeled region or sulcus.

900

901 We organized the data in a nested fashion: brain hemisphere is nested within subject, and subject is  
902 nested within laboratory. In addition to the five shape measurements and the three nested classification  
903 factors, the data also include three covariates: sex (male, female), age (integer variable), and handedness  
904 (left, right; we relabeled two ambidextrous subjects as left-handed). Given the grouped nature of the  
905 data, we used linear mixed models for the statistical modeling of the data. To assess the importance of  
906 each of the covariates and nested classification factors, we fitted 24 distinct linear mixed models for  
907 each shape measure and brain region combination to assess the importance of each of the covariates  
908 (sex, handedness, and age as fixed effects) and nested classification factors (laboratory, subject, and  
909 brain hemisphere as random effects). For each shape measure, we decomposed the total variance into the  
910 variance between laboratories, between subjects within a laboratory, between brain hemispheres within a  
911 subject, and within brain hemispheres.

912

913 For each shape measure and brain region combination, we used the Bayesian Information Criterion  
914 (BIC) score to select the best model among the 24 competing models. A BIC score is a goodness of fit  
915 measure used to perform model selection among models with different dimensions (number of  
916 parameters), and is proportional to the negative log likelihood of the model penalized by the number of  
917 parameters in the model. It strikes a balance between model fit (measured by the log-likelihood score)

918 and model complexity (measured by the number of parameters in the model). In the context of linear  
919 models, an over-parameterized model will always have a larger log-likelihood score than a more  
920 parsimonious model, but it will also likely overfit the data. Nonetheless, by including a penalty  
921 proportional to the number of parameters in the model, the BIC score can be used to compare models  
922 with different dimensions since over-parameterized models are penalized to a greater extent. The smaller  
923 the BIC score, the better the model fits the data.

924

925 Two models stood out as the best models for the mean curvature, travel depth, FreeSurfer convexity, and  
926 FreeSurfer thickness shape measures across the 31 brain regions (**Supplement 2**). Both models include  
927 handedness and age as fixed effects. They only differ by the inclusion of the extra “subject within lab”  
928 nesting level. For all shape measures and brain regions, the bulk of the variability was concentrated in  
929 the residual, not in the hemisphere (“side”), subject, or laboratory (top of **Fig 14**).

930

931 **Fig 14. Brain shape variation in healthy humans.**

932 Top: Overview of the variance results for five shape measures computed on each of 31 manually labeled  
933 cortical regions (combined across both hemispheres for this figure) in the 101 Mindboggle-101 healthy  
934 human brains. The table shows the relative contributions of subject, hemisphere, and residual to describe  
935 the variability for each shape measure, with a greater contribution coded by a darker blue. For all shape  
936 measures and brain regions, most of the variability was concentrated in the residual. See **Supplement 2**  
937 for a description of the statistical models. Bottom: An example heatmap table containing 4,848 cells,  
938 where each cell is color-coded (increasing from red to yellow) to represent the median absolute  
939 deviation of travel depth values across all vertices in each of 48 sulcus surface meshes for the 101  
940 subjects.

941

942 We repeated the same analysis as above on two scans acquired three years apart from hundreds of the  
943 ADNI participants (126 with Alzheimer’s, 199 healthy controls) as part of an international Alzheimer’s  
944 challenge (see Section 2.1: 2015 above) to see if we could find changes in brain shape measures that  
945 correlate with changes in ADNI-MEM cognitive scores over the course of three years. This resulted in  
946 the most detailed shape analysis of brains with Alzheimer’s disease ever conducted [118]  
947 (<https://osf.io/d7hx8/>). To identify shape measures associated with Alzheimer’s disease, we used the

948 average of the ranks of the following tests in that study: Kolmogorov-Smirnov test to see if there was a  
949 difference between distributions at baseline and at three years, and correlation of change in shape and  
950 change in ADNI-MEM cognitive scores.

951

952 We found that healthy brains and brains with Alzheimer's disease have similar shape statistical  
953 summaries, but changes in the following shape measures after a three-year interval were significantly  
954 correlated with changes in ADNI-MEM cognitive score:

955

- 956 ● Volume for right caudal anterior cingulate and left: entorhinal, inferior parietal, (middle,  
957 superior) temporal, superior frontal, precuneus, and supramarginal gyri
- 958 ● FreeSurfer thickness for left and right: entorhinal, fusiform, inferior parietal, (inferior, middle,  
959 superior) temporal, superior frontal, precuneus, and supramarginal gyri; left: (caudal  
960 middle/lateral, orbito/rostral middle) frontal, and pars triangularis gyri; right lingual gyrus
- 961 ● Mean curvature for left and right rostral middle frontal gyri; left (middle, superior) temporal  
962 gyri; right inferior temporal gyri

963

964

965

966

## 967 **4. Discussion**

968 In this article, we have documented the Mindboggle open source brain morphometry platform and  
969 demonstrated its use in studies of shape variation in healthy and diseased humans. The number of  
970 different shape measures and the size of the populations make this the largest and most detailed shape  
971 analysis of human brains ever conducted. There are many ways in which the open source software  
972 community can extend Mindboggle's capabilities, and there are many possible applications for  
973 Mindboggle to brain and non-brain data. Here we will very briefly summarize this article's results and  
974 point toward possible further evaluations and alternative approaches.

975

### 976 **4.1. Summary of results**

977 In this section we summarize the findings of our evaluations in the Results section. Shape measures are  
978 not independent of one another, and some related shape measures exaggerate values for certain  
979 morphological structures (such as geodesic vs. travel depth for the insula). Mindboggle's thickinthehead  
980 cortical thickness measure is consistent across scans and across brains and generated values that are  
981 closer to published ranges of values than FreeSurfer or ANTs values. Mindboggle's travel depth  
982 measure provides a more faithful representation of depth for shallow portions than FreeSurfer's  
983 convexity measure. Mindboggle's fundi are comparable to Gang Li's fundi in terms of average  
984 proximity to manual label boundaries, but there was no clear winner in our evaluation of fundus  
985 extraction algorithms. Mindboggle's shape measures are reasonably consistent across scans of the same  
986 brain, with some exceptions (such as entorhinal volume). We found that for the shape measures and  
987 populations we studied that shape differences between hemispheres were greater than shape differences  
988 between MRI scans of the same hemisphere, and that the variability within each brain hemisphere was  
989 higher than the variability between brain hemispheres in a participant or between participants. Finally,  
990 we reported which brain regions were significantly correlated with changes in ADNI-MEM cognitive

991 score after a three-year interval as part of an international Alzheimer's challenge.

992

#### 993 **4.2. Further evaluations and enhancements of Mindboggle**

994 The Mindboggle software will continue to be subjected to evaluations of its algorithms as well as of its  
995 applicability to new datasets of healthy and diseased brains. Data exist to conduct evaluations of  
996 test/retest reliability and reproducibility [119,120], with different imaging parameters [121], with genetic  
997 information [122], with heritability information [123], at higher field strengths [124], etc. Some data  
998 also exist for evaluating features such as sulcal pits [125]. Including different types of brain images can  
999 enable multivariate analyses, independent corroboration of morphology, and can even help to better  
1000 interpret the factors that influence morphology [79]. We also intend to evaluate Mindboggle output by  
1001 analyzing interactions among shape measures to find higher order morphological relationships with  
1002 brain shape differences.

1003

1004 There are many ways to enhance Mindboggle's functionality and applicability to pathological brains.  
1005 Taking advantage of different and multiple types of images, atlases, labels, features, and shape measures  
1006 are clear ways to expand and improve Mindboggle, and the software was built using the Nipype  
1007 framework specifically to enable modular and flexible inclusion of different algorithms. Even the inputs  
1008 to Mindboggle can change to take advantage of promising new algorithms that combine surface  
1009 reconstruction with whole-brain segmentation in a way that is more robust to white-matter abnormalities  
1010 [126]. Use of probabilistic labels, features, and shape measures could lead to more careful  
1011 interpretations of morphometry studies.

1012

#### 1013 **4.3. Alternative approaches to Mindboggle: Deep learning and beyond**

1014 The Mindboggle software extracts and identifies features for shape analysis. This approach is based on  
1015 human-designed features (brain structure and label definitions and algorithmic implementations) and

1016 assumes the validity of the designed feature model. The tremendous success that machine learning  
1017 (especially deep learning) approaches have had across domains [127] are strong evidence that such  
1018 approaches may improve automated feature extraction, identification and labeling for features that a  
1019 human would never consider designing. Machine learning has recently been demonstrated to recognize  
1020 the multi-modal ‘fingerprint’ of cortical areas [24]. In 2011, we advocated a novel application of  
1021 convolutional networks to build discriminative features and were able to demonstrate automated  
1022 volumetric labeling of the cerebral cortex, without human intervention to build handcrafted features or  
1023 to provide other prior knowledge [128]. At the time we had very limited training data (40 manually  
1024 labeled brains), but with the Mindboggle-101 dataset, tables of shape statistics generated by  
1025 Mindboggle, and with improved deep learning architectures, we may now be in a better position to apply  
1026 deep learning to this problem. It may be helpful to explore ways in which priors and invariances can be  
1027 modeled and integrated into deep learning approaches to reduce the amount of required training data and  
1028 to integrate human expert information. This may be particularly beneficial for pathological conditions  
1029 with tumors, lesions, and edemas, etc. that do not conform to a canonical reference brain or are difficult  
1030 to obtain in sufficient quantities to train a deep learning algorithm. Indeed, thousands or millions of  
1031 curated and labeled examples are usually required for deep learning algorithms, which points to the  
1032 promise of unsupervised approaches that do not require expert feedback during training and can learn  
1033 from messier data or from less data. Combining algorithmic approaches to feature extraction and  
1034 morphometry with machine learning and unsupervised approaches has great potential applications in  
1035 characterizing not just healthy human brain variation but in diagnosing, tracking, and predicting  
1036 unhealthy conditions.

1037

1038

1039 **Supporting Information**

1040

1041 **Document S1. Travel depth**

1042

1043 **Document S2. Variance components analysis of the shapes of 62 cortical regions in 101 human**

1044 **brains**

1045

1046 **Appendix S3. Mindboggle output directory tree**

1047

1048

1049 **Acknowledgments**

1050 We sincerely thank everyone who has contributed to the Mindboggle open science project over the  
1051 years, including Nolan Nichols, Oliver Hinds, Arthur Mikhno, Hal Canary, and Ben Cipollini. We also  
1052 thank Gang Li, Denis Rivière, and Olivier Coulon for assistance with the fundus evaluation. Arno Klein  
1053 would like to thank Deepanjana and Ellora for their continued patience and support, and dedicates this  
1054 project to his mother and father, Karen and Arnold Klein.

1055

1056 Software and online resources that have benefitted the project include: GitHub.com, ReadtheDocs.org,  
1057 and PyCharm for software development; Open Science Framework, Harvard Dataverse, and  
1058 Synapse.org for public data storage; and D3, Bokeh, Paraview, and the Viridis colormap  
1059 (<https://github.com/bids/colormap>) for visualization.

1060

1061 **Author Contributions**

1062 Arno Klein led the development of the project, organized the studies, was the main contributor to the  
1063 software, and wrote the manuscript. Satrajit S. Ghosh contributed to the development of the software  
1064 pipeline framework, has provided invaluable guidance over the years, and led the consulting group  
1065 TankThink Lab's involvement in the project. Forrest S. Bao wrote an early version of the software for

1066 extracting morphological features from brain surfaces and an open source Python version of Martin  
1067 Reuter's Laplace-Beltrami code. Joachim Giard wrote the open source C++ software for measuring  
1068 depth and curvature along brain surfaces. Yrjö Häme explored hidden Markov measure field-based  
1069 feature extraction. Eliezer Stavsky performed early explorations into surface feature-based label  
1070 propagation. Noah Lee contributed to the original R01 proposal that supported Mindboggle's research  
1071 efforts, created an early graph-based database with interactive visualization, and implemented a deep  
1072 learning approach to automate anatomical labeling. Martin Reuter helped to port his Laplace-Beltrami  
1073 spectral shape measure to Python and evaluate the code. Elias Chaibub Neto performed statistical  
1074 analyses of shape variation. Anisha Keshavan is helping to develop the ROYGBIV interactive online  
1075 brain image viewer for visualizing Mindboggle output.

1076

## 1077 **References**

- 1078 1. Paulus MP, Tapert SF, Schuckit MA. Neural activation patterns of methamphetamine-dependent  
1079 subjects during decision making predict relapse. *Arch Gen Psychiatry* [Internet]. 2005  
1080 Jul;62(7):761–8. Available from: <http://dx.doi.org/10.1001/archpsyc.62.7.761>
- 1081 2. Koutsouleris N, Meisenzahl EM, Davatzikos C, Bottlender R, Frodl T, Scheuerecker J, et al. Use of  
1082 neuroanatomical pattern classification to identify subjects in at-risk mental states of psychosis and  
1083 predict disease transition. *Arch Gen Psychiatry* [Internet]. 2009 Jul [cited 2016 Aug 6];66(7):700–  
1084 12. Available from: <http://dx.doi.org/10.1001/archgenpsychiatry.2009.62>
- 1085 3. Whalley HC, Simonotto E, Moorhead W, McIntosh A, Marshall I, Ebmeier KP, et al. Functional  
1086 imaging as a predictor of schizophrenia. *Biol Psychiatry* [Internet]. 2006 Sep 1 [cited 2016 Aug  
1087 6];60(5):454–62. Available from: <http://dx.doi.org/10.1016/j.biopsych.2005.11.013>
- 1088 4. Canli T, Cooney RE, Goldin P, Shah M, Sivers H, Thomason ME, et al. Amygdala reactivity to  
1089 emotional faces predicts improvement in major depression. *Neuroreport* [Internet]. 2005 Aug  
1090 22;16(12):1267–70. Available from: <http://www.ncbi.nlm.nih.gov/pubmed/16056122>
- 1091 5. Chen C-H, Ridler K, Suckling J, Williams S, Fu CHY, Merlo-Pich E, et al. Brain imaging  
1092 correlates of depressive symptom severity and predictors of symptom improvement after  
1093 antidepressant treatment. *Biol Psychiatry* [Internet]. 2007 Sep 1 [cited 2016 Aug 6];62(5):407–14.  
1094 Available from: <http://dx.doi.org/10.1016/j.biopsych.2006.09.018>
- 1095 6. Fu CHY, Williams SCR, Brammer MJ, Suckling J, Kim J, Cleare AJ, et al. Neural responses to  
1096 happy facial expressions in major depression following antidepressant treatment. *Am J Psychiatry*  
1097 [Internet]. 2007 Apr [cited 2016 Aug 6];164(4):599–607. Available from:

- 1098 <http://dx.doi.org/10.1176/ajp.2007.164.4.599>
- 1099 7. Nitschke JB, Sarinopoulos I, Oathes DJ, Johnstone T, Whalen PJ, Davidson RJ, et al. Anticipatory  
1100 activation in the amygdala and anterior cingulate in generalized anxiety disorder and prediction of  
1101 treatment response. *Am J Psychiatry* [Internet]. 2009 Mar [cited 2016 Aug 6];166(3):302–10.  
1102 Available from: <http://dx.doi.org/10.1176/appi.ajp.2008.07101682>
- 1103 8. Kumari V, Peters ER, Fannon D, Antonova E, Premkumar P, Anilkumar AP, et al. Dorsolateral  
1104 prefrontal cortex activity predicts responsiveness to cognitive-behavioral therapy in schizophrenia.  
1105 *Biol Psychiatry* [Internet]. 2009 Sep 15 [cited 2016 Aug 6];66(6):594–602. Available from:  
1106 <http://dx.doi.org/10.1016/j.biopsych.2009.04.036>
- 1107 9. Doehrmann O, Ghosh SS, Polli FE, Reynolds GO, Horn F, Keshavan A, et al. Predicting treatment  
1108 response in social anxiety disorder from functional magnetic resonance imaging. *JAMA Psychiatry*  
1109 [Internet]. 2013 Jan;70(1):87–97. Available from: <http://dx.doi.org/10.1001/2013.jamapsychiatry.5>
- 1110 10. Whitfield-Gabrieli S, Ghosh SS, Nieto-Castanon A, Saygin Z, Doehrmann O, Chai XJ, et al. Brain  
1111 connectomics predict response to treatment in social anxiety disorder. *Mol Psychiatry* [Internet].  
1112 2015 Aug 11; Available from: <http://dx.doi.org/10.1038/mp.2015.109>
- 1113 11. Gabrieli JDE, Ghosh SS, Whitfield-Gabrieli S. Prediction as a humanitarian and pragmatic  
1114 contribution from human cognitive neuroscience. *Neuron* [Internet]. 2015 Jan 7;85(1):11–26.  
1115 Available from: <http://dx.doi.org/10.1016/j.neuron.2014.10.047>
- 1116 12. Insel TR, Cuthbert BN. Endophenotypes: bridging genomic complexity and disorder heterogeneity.  
1117 *Biol Psychiatry* [Internet]. 2009 Dec 1 [cited 2016 Aug 6];66(11):988–9. Available from:  
1118 <http://dx.doi.org/10.1016/j.biopsych.2009.10.008>
- 1119 13. Crum WR, Camara O, Rueckert D, Bhatia KK, Jenkinson M, Hill DLG. Generalised overlap  
1120 measures for assessment of pairwise and groupwise image registration and segmentation. In:  
1121 *Medical Image Computing and Computer-Assisted Intervention–MICCAI 2005* [Internet].  
1122 Springer; 2005 [cited 2015 Oct 10]. p. 99–106. Available from:  
1123 [http://link.springer.com/chapter/10.1007/11566465\\_13](http://link.springer.com/chapter/10.1007/11566465_13)
- 1124 14. Devlin JT, Poldrack RA. In praise of tedious anatomy. *Neuroimage* [Internet]. 2007 Oct 1 [cited  
1125 2016 Aug 6];37(4):1033–41; discussion 1050–8. Available from:  
1126 <http://dx.doi.org/10.1016/j.neuroimage.2006.09.055>
- 1127 15. Bohland JW, Bokil H, Allen CB, Mitra PP. The brain atlas concordance problem: quantitative  
1128 comparison of anatomical parcellations. Sporns O, editor. *PLoS One* [Internet]. 2009 Sep 29 [cited  
1129 2016 Aug 6];4(9):e7200. Available from: <http://dx.doi.org/10.1371/journal.pone.0007200>
- 1130 16. Klein A, Andersson J, Ardekani BA, Ashburner J, Avants B, Chiang M-C, et al. Evaluation of 14  
1131 nonlinear deformation algorithms applied to human brain MRI registration. *Neuroimage* [Internet].  
1132 2009 Jul 1 [cited 2016 Aug 6];46(3):786–802. Available from:  
1133 <http://dx.doi.org/10.1016/j.neuroimage.2008.12.037>
- 1134 17. Avants B, Klein A, Tustison N, Wu J, Gee JC. Evaluation of open-access, automated brain  
1135 extraction methods on multi-site multi-disorder data. In: 16th annual meeting for the Organization  
1136 of Human Brain Mapping. 2010.

- 1137 18. Klein A, Ghosh SS, Avants B, Yeo BTT, Fischl B, Ardekani B, et al. Evaluation of volume-based  
1138 and surface-based brain image registration methods. *Neuroimage* [Internet]. 2010 May 15 [cited  
1139 2016 Aug 6];51(1):214–20. Available from: <http://dx.doi.org/10.1016/j.neuroimage.2010.01.091>
- 1140 19. Klein A, Hirsch J. Mindboggle: a scatterbrained approach to automate brain labeling. *Neuroimage*  
1141 [Internet]. 2005 Jan 15;24(2):261–80. Available from:  
1142 <http://dx.doi.org/10.1016/j.neuroimage.2004.09.016>
- 1143 20. Rogelj P, Kovacic S, Gee JC. Validation of a nonrigid registration algorithm for multimodal data.  
1144 In: Sonka M, Fitzpatrick JM, editors. *Medical Imaging 2002* [Internet]. International Society for  
1145 Optics and Photonics; 2002 [cited 2016 Aug 6]. p. 299–307. Available from:  
1146 <http://proceedings.spiedigitallibrary.org/proceeding.aspx?doi=10.1117/12.467170>
- 1147 21. Rademacher J, Caviness VS Jr, Steinmetz H, Galaburda AM. Topographical variation of the human  
1148 primary cortices: implications for neuroimaging, brain mapping, and neurobiology. *Cereb Cortex*  
1149 [Internet]. 1993 Jul [cited 2016 Aug 6];3(4):313–29. Available from:  
1150 <http://www.ncbi.nlm.nih.gov/pubmed/8400809>
- 1151 22. Klein A, Tourville J. 101 labeled brain images and a consistent human cortical labeling protocol.  
1152 *Front Neurosci* [Internet]. 2012 Dec 5 [cited 2016 Aug 6];6:171. Available from:  
1153 <http://dx.doi.org/10.3389/fnins.2012.00171>
- 1154 23. Klein A, Dal Canton T, Ghosh SS, Landman B, Worth A. Open labels: online feedback for a public  
1155 resource of manually labeled brain images. In: 16th annual meeting for the Organization of Human  
1156 Brain Mapping [Internet]. 2010. Available from:  
1157 <https://mfr.osf.io/render?url=https://osf.io/tmjbn/?action=download%26mode=render>
- 1158 24. Glasser MF, Coalson TS, Robinson EC, Hacker CD, Harwell J, Yacoub E, et al. A multi-modal  
1159 parcellation of human cerebral cortex. *Nature* [Internet]. 2016 Jul 20; Available from:  
1160 <http://dx.doi.org/10.1038/nature18933>
- 1161 25. Régis J, Mangin J-F, Ochiai T, Frouin V, Rivière D, Cachia A, et al. “Sulcal root” generic model: a  
1162 hypothesis to overcome the variability of the human cortex folding patterns. *Neurol Med Chir*  
1163 [Internet]. 2005 Jan;45(1):1–17. Available from: <http://www.ncbi.nlm.nih.gov/pubmed/15699615>
- 1164 26. Lohmann G, von Cramon DY, Colchester ACF. Deep sulcal landmarks provide an organizing  
1165 framework for human cortical folding. *Cereb Cortex* [Internet]. 2008 Jun [cited 2016 Aug  
1166 6];18(6):1415–20. Available from: <http://dx.doi.org/10.1093/cercor/bhm174>
- 1167 27. Meng Y, Li G, Lin W, Gilmore JH, Shen D. Spatial distribution and longitudinal development of  
1168 deep cortical sulcal landmarks in infants. *Neuroimage* [Internet]. 2014 Oct 15 [cited 2016 Aug  
1169 6];100:206–18. Available from: <http://dx.doi.org/10.1016/j.neuroimage.2014.06.004>
- 1170 28. Perrot M, Rivière D, Mangin J-F. Cortical sulci recognition and spatial normalization. *Med Image*  
1171 *Anal.* 2011 Aug;15(4):529–50.
- 1172 29. Dryden IL, Mardia KV. *Statistical shape analysis*. 1998; Available from:  
1173 <https://pdfs.semanticscholar.org/6ba2/73a7cfa282f73423110d00a5d20ad36766e1.pdf>
- 1174 30. Bansal R, Staib LH, Laine AF, Hao X, Xu D, Liu J, et al. Anatomical brain images alone can  
1175 accurately diagnose chronic neuropsychiatric illnesses. *PLoS One* [Internet]. 2012 Dec

- 1176 7;7(12):e50698. Available from: <http://dx.doi.org/10.1371/journal.pone.0050698>
- 1177 31. Lerch JP, Pruessner J, Zijdenbos AP, Collins DL, Teipel SJ, Hampel H, et al. Automated cortical  
1178 thickness measurements from MRI can accurately separate Alzheimer's patients from normal  
1179 elderly controls. *Neurobiol Aging* [Internet]. 2008 Jan [cited 2016 Aug 6];29(1):23–30. Available  
1180 from: <http://dx.doi.org/10.1016/j.neurobiolaging.2006.09.013>
- 1181 32. Im K, Lee J-M, Seo SW, Hyung Kim S, Kim SI, Na DL. Sulcal morphology changes and their  
1182 relationship with cortical thickness and gyral white matter volume in mild cognitive impairment  
1183 and Alzheimer's disease. *Neuroimage* [Internet]. 2008 Oct 15 [cited 2016 Aug 6];43(1):103–13.  
1184 Available from: <http://dx.doi.org/10.1016/j.neuroimage.2008.07.016>
- 1185 33. Julkunen V, Niskanen E, Koikkalainen J, Herukka S-K, Pihlajamäki M, Hallikainen M, et al.  
1186 Differences in cortical thickness in healthy controls, subjects with mild cognitive impairment, and  
1187 Alzheimer's disease patients: a longitudinal study. *J Alzheimers Dis* [Internet]. 2010;21(4):1141–  
1188 51. Available from: <http://www.ncbi.nlm.nih.gov/pubmed/21504134>
- 1189 34. Steenwijk MD, Geurts JJG, Daams M, Tijms BM, Wink AM, Balk LJ, et al. Cortical atrophy  
1190 patterns in multiple sclerosis are non-random and clinically relevant. *Brain* [Internet]. 2016 Jan  
1191 [cited 2016 Aug 6];139(Pt 1):115–26. Available from: <http://dx.doi.org/10.1093/brain/awv337>
- 1192 35. Kuperberg GR, Broome MR, McGuire PK, David AS, Eddy M, Ozawa F, et al. Regionally  
1193 localized thinning of the cerebral cortex in schizophrenia. *Arch Gen Psychiatry* [Internet]. 2003  
1194 Sep;60(9):878–88. Available from: <http://dx.doi.org/10.1001/archpsyc.60.9.878>
- 1195 36. Jiao Y, Chen R, Ke X, Chu K, Lu Z, Herskovits EH. Predictive models of autism spectrum disorder  
1196 based on brain regional cortical thickness. *Neuroimage* [Internet]. 2010 Apr 1 [cited 2016 Aug  
1197 6];50(2):589–99. Available from: <http://dx.doi.org/10.1016/j.neuroimage.2009.12.047>
- 1198 37. Durazzo TC, Tosun D, Buckley S, Gazdzinski S, Mon A, Fryer SL, et al. Cortical thickness,  
1199 surface area, and volume of the brain reward system in alcohol dependence: relationships to relapse  
1200 and extended abstinence. *Alcohol Clin Exp Res* [Internet]. 2011 Jun [cited 2016 Aug  
1201 6];35(6):1187–200. Available from: <http://dx.doi.org/10.1111/j.1530-0277.2011.01452.x>
- 1202 38. Bakkour A, Morris JC, Dickerson BC. The cortical signature of prodromal AD: regional thinning  
1203 predicts mild AD dementia. *Neurology* [Internet]. 2009 Mar 24 [cited 2016 Aug 6];72(12):1048–  
1204 55. Available from: <http://dx.doi.org/10.1212/01.wnl.0000340981.97664.2f>
- 1205 39. Querbes O, Aubry F, Pariente J, Lotterie J-A, Démonet J-F, Duret V, et al. Early diagnosis of  
1206 Alzheimer's disease using cortical thickness: impact of cognitive reserve. *Brain* [Internet]. 2009  
1207 Aug [cited 2016 Aug 6];132(Pt 8):2036–47. Available from:  
1208 <http://dx.doi.org/10.1093/brain/awp105>
- 1209 40. Eskildsen SF, Coupé P, García-Lorenzo D, Fonov V, Pruessner JC, Collins DL, et al. Prediction of  
1210 Alzheimer's disease in subjects with mild cognitive impairment from the ADNI cohort using  
1211 patterns of cortical thinning. *Neuroimage* [Internet]. 2013 Jan 15 [cited 2016 Aug 6];65:511–21.  
1212 Available from: <http://dx.doi.org/10.1016/j.neuroimage.2012.09.058>
- 1213 41. Wee C-Y, Yap P-T, Shen D, Alzheimer's Disease Neuroimaging Initiative. Prediction of  
1214 Alzheimer's disease and mild cognitive impairment using cortical morphological patterns. *Hum*  
1215 *Brain Mapp* [Internet]. 2013 Dec [cited 2016 Aug 6];34(12):3411–25. Available from:

- 1216 <http://dx.doi.org/10.1002/hbm.22156>
- 1217 42. Wei R, Li C, Fogelson N, Li L. Prediction of Conversion from Mild Cognitive Impairment to  
1218 Alzheimer's Disease Using MRI and Structural Network Features. *Front Aging Neurosci* [Internet].  
1219 2016 Apr 19 [cited 2016 Aug 6];8:76. Available from: <http://dx.doi.org/10.3389/fnagi.2016.00076>
- 1220 43. Dickerson BC, Wolk DA, Alzheimer's Disease Neuroimaging Initiative. MRI cortical thickness  
1221 biomarker predicts AD-like CSF and cognitive decline in normal adults. *Neurology* [Internet]. 2012  
1222 Jan 10;78(2):84–90. Available from: <http://dx.doi.org/10.1212/WNL.0b013e31823efc6c>
- 1223 44. Latha V, Petroula P, Eric W, J-Sebastian M, Patrizia M, Bruno V, et al. Entorhinal Cortex  
1224 Thickness Predicts Cognitive Decline in Alzheimer's Disease. *J Alzheimers Dis* [Internet]. 2013  
1225 [cited 2016 Aug 6];(3):755–66. Available from:  
1226 [http://www.medra.org/servlet/aliasResolver?alias=iospress&genre=article&issn=1387-](http://www.medra.org/servlet/aliasResolver?alias=iospress&genre=article&issn=1387-2877&volume=33&issue=3&spage=755&doi=10.3233/JAD-2012-121408)  
1227 [2877&volume=33&issue=3&spage=755&doi=10.3233/JAD-2012-121408](http://www.medra.org/servlet/aliasResolver?alias=iospress&genre=article&issn=1387-2877&volume=33&issue=3&spage=755&doi=10.3233/JAD-2012-121408)
- 1228 45. Foland-Ross LC, Sacchet MD, Prasad G, Gilbert B, Thompson PM, Gotlib IH. Cortical thickness  
1229 predicts the first onset of major depression in adolescence. *Int J Dev Neurosci* [Internet]. 2015 Nov  
1230 [cited 2016 Aug 6];46:125–31. Available from: <http://dx.doi.org/10.1016/j.ijdevneu.2015.07.007>
- 1231 46. Shaw P, Lerch J, Greenstein D, Sharp W, Clasen L, Evans A, et al. Longitudinal mapping of  
1232 cortical thickness and clinical outcome in children and adolescents with attention-  
1233 deficit/hyperactivity disorder. *Arch Gen Psychiatry* [Internet]. 2006 May;63(5):540–9. Available  
1234 from: <http://dx.doi.org/10.1001/archpsyc.63.5.540>
- 1235 47. Ecker C, Marquand A, Mourão-Miranda J, Johnston P, Daly EM, Brammer MJ, et al. Describing  
1236 the brain in autism in five dimensions--magnetic resonance imaging-assisted diagnosis of autism  
1237 spectrum disorder using a multiparameter classification approach. *J Neurosci* [Internet]. 2010 Aug  
1238 11 [cited 2016 Aug 6];30(32):10612–23. Available from:  
1239 <http://dx.doi.org/10.1523/JNEUROSCI.5413-09.2010>
- 1240 48. Cointepas Y, Mangin J-F, Garnero L, Poline J-B, Benali H. BrainVISA: Software platform for  
1241 visualization and analysis of multi-modality brain data. *Neuroimage* [Internet]. 2001/6 [cited 2016  
1242 Aug 6];13(6, Supplement):98. Available from:  
1243 <http://www.sciencedirect.com/science/article/pii/S1053811901914417>
- 1244 49. Kochunov P, Rogers W, Mangin J-F, Lancaster J. A library of cortical morphology analysis tools to  
1245 study development, aging and genetics of cerebral cortex. *Neuroinformatics* [Internet]. 2012 Jan  
1246 [cited 2016 Aug 6];10(1):81–96. Available from: <http://dx.doi.org/10.1007/s12021-011-9127-9>
- 1247 50. Liu T, Sachdev PS, Lipnicki DM, Jiang J, Cui Y, Kochan NA, et al. Longitudinal changes in sulcal  
1248 morphology associated with late-life aging and MCI. *Neuroimage* [Internet]. 2013 Jul 1 [cited 2016  
1249 Aug 6];74:337–42. Available from: <http://dx.doi.org/10.1016/j.neuroimage.2013.02.047>
- 1250 51. Cachia A, Paillère-Martinot M-L, Galinowski A, Januel D, de Beaupaire R, Bellivier F, et al.  
1251 Cortical folding abnormalities in schizophrenia patients with resistant auditory hallucinations.  
1252 *Neuroimage* [Internet]. 2008 Feb 1 [cited 2016 Aug 6];39(3):927–35. Available from:  
1253 <http://dx.doi.org/10.1016/j.neuroimage.2007.08.049>
- 1254 52. Penttilä J, Cachia A, Martinot J-L, Ringuenet D, Wessa M, Houenou J, et al. Cortical folding  
1255 difference between patients with early-onset and patients with intermediate-onset bipolar disorder.

- 1256 Bipolar Disord [Internet]. 2009 Jun [cited 2016 Aug 6];11(4):361–70. Available from:  
1257 <http://dx.doi.org/10.1111/j.1399-5618.2009.00683.x>
- 1258 53. Mangin J-F, Jouvent E, Cachia A. In-vivo measurement of cortical morphology: means and  
1259 meanings. *Curr Opin Neurol* [Internet]. 2010 Aug [cited 2016 Aug 6];23(4):359–67. Available  
1260 from: <http://dx.doi.org/10.1097/WCO.0b013e32833a0afc>
- 1261 54. Kempton MJ, Salvador Z, Munafò MR, Geddes JR, Simmons A, Frangou S, et al. Structural  
1262 neuroimaging studies in major depressive disorder. Meta-analysis and comparison with bipolar  
1263 disorder. *Arch Gen Psychiatry* [Internet]. 2011 Jul [cited 2016 Aug 6];68(7):675–90. Available  
1264 from: <http://dx.doi.org/10.1001/archgenpsychiatry.2011.60>
- 1265 55. Mikhno A, Nuevo PM, Devanand DP, Parsey RV, Laine AF. Multimodal classification of  
1266 Dementia using functional data, anatomical features and 3D invariant shape descriptors. In: 2012  
1267 9th IEEE International Symposium on Biomedical Imaging (ISBI) [Internet]. IEEE; 2012 [cited  
1268 2016 Aug 6]. p. 606–9. Available from: <http://dx.doi.org/10.1109/ISBI.2012.6235621>
- 1269 56. Gorgolewski K, Burns CD, Madison C, Clark D, Halchenko YO, Waskom ML, et al. Nipype: a  
1270 flexible, lightweight and extensible neuroimaging data processing framework in python. *Front*  
1271 *Neuroinform* [Internet]. 2011 Aug 22 [cited 2016 Aug 6];5:13. Available from:  
1272 <http://dx.doi.org/10.3389/fninf.2011.00013>
- 1273 57. Klein A. Automated brain labeling with Mindboggle. [New York, NY]: Cornell University; 2004.
- 1274 58. Klein A, Mensh B, Ghosh S, Tourville J, Hirsch J. Mindboggle: automated brain labeling with  
1275 multiple atlases. *BMC Med Imaging* [Internet]. 2005 Oct 5;5:7. Available from:  
1276 <http://dx.doi.org/10.1186/1471-2342-5-7>
- 1277 59. Caviness VS Jr, Meyer J, Makris N, Kennedy DN. MRI-Based Topographic Parcellation of Human  
1278 Neocortex: An Anatomically Specified Method with Estimate of Reliability. *J Cogn Neurosci*  
1279 [Internet]. 1996 Nov [cited 2016 Aug 6];8(6):566–87. Available from:  
1280 <http://dx.doi.org/10.1162/jocn.1996.8.6.566>
- 1281 60. Klein, Arno. Mindboggle-101 manually labeled individual brains [Internet]. Harvard Dataverse;  
1282 2016 [cited 2016 Aug 6]. Available from: <http://dx.doi.org/10.7910/DVN/HMQKCK>
- 1283 61. Klein, Arno. Mindboggle-101 templates (unlabeled images from a population of brains) [Internet].  
1284 Harvard Dataverse; 2016 [cited 2016 Aug 6]. Available from:  
1285 <http://dx.doi.org/10.7910/DVN/WDIYB5>
- 1286 62. Klein, Arno. Mindboggle-101 atlases (anatomical labels from a population of brains) [Internet].  
1287 Harvard Dataverse; 2016 [cited 2016 Aug 6]. Available from:  
1288 <http://dx.doi.org/10.7910/DVN/XCCE9Q>
- 1289 63. Wang H, Yushkevich PA. Multi-atlas segmentation with joint label fusion and corrective learning-  
1290 an open source implementation. *Front Neuroinform* [Internet]. 2013 Nov 22 [cited 2016 Aug  
1291 6];7:27. Available from: <http://dx.doi.org/10.3389/fninf.2013.00027>
- 1292 64. Dale AM, Fischl B, Sereno MI. Cortical surface-based analysis. I. Segmentation and surface  
1293 reconstruction. *Neuroimage* [Internet]. 1999 Feb [cited 2016 Aug 6];9(2):179–94. Available from:  
1294 <http://dx.doi.org/10.1006/nimg.1998.0395>

- 1295 65. Fischl B, Sereno MI, Dale AM. Cortical surface-based analysis. II: Inflation, flattening, and a  
1296 surface-based coordinate system. *Neuroimage* [Internet]. 1999 Feb [cited 2016 Aug 6];9(2):195–  
1297 207. Available from: <http://dx.doi.org/10.1006/nimg.1998.0396>
- 1298 66. Fischl B, Sereno MI, Tootell RB, Dale AM. High-resolution intersubject averaging and a  
1299 coordinate system for the cortical surface. *Hum Brain Mapp* [Internet]. 1999;8(4):272–84.  
1300 Available from: <http://www.ncbi.nlm.nih.gov/pubmed/10619420>
- 1301 67. Klein A, Bao FS, Hame Y, Stavsky E, Giard J, Haehn D, et al. Mindboggle: Automated human  
1302 brain MRI feature extraction, labeling, morphometry, and online visualization. In:  
1303 *Neuroinformatics* [Internet]. 2012. Available from: <http://f1000research.com/f1000posters/1092565>
- 1304 68. Arno K, Nolan N, Daniel H. Mindboggle 2 interface: online visualization of extracted brain  
1305 features with XTK. *Front Neuroinform* [Internet]. 2014 [cited 2016 Aug 6];8. Available from:  
1306 [http://www.frontiersin.org/Community/AbstractDetails.aspx?ABS\\_DOI=10.3389/conf.fninf.2014.0](http://www.frontiersin.org/Community/AbstractDetails.aspx?ABS_DOI=10.3389/conf.fninf.2014.08.00086)  
1307 [8.00086](http://www.frontiersin.org/Community/AbstractDetails.aspx?ABS_DOI=10.3389/conf.fninf.2014.08.00086)
- 1308 69. Keshavan A, Klein A, Cipollini B. Interactive online brain shape visualization [Internet]. 2016  
1309 Aug. Available from: <http://biorxiv.org/lookup/doi/10.1101/067678>
- 1310 70. Jack CR Jr, Bernstein MA, Fox NC, Thompson P, Alexander G, Harvey D, et al. The Alzheimer’s  
1311 Disease Neuroimaging Initiative (ADNI): MRI methods. *J Magn Reson Imaging* [Internet]. 2008  
1312 Apr [cited 2016 Aug 6];27(4):685–91. Available from: <http://dx.doi.org/10.1002/jmri.21049>
- 1313 71. Simmons A, Westman E, Muehlboeck S, Mecocci P, Vellas B, Tsolaki M, et al. MRI measures of  
1314 Alzheimer’s disease and the AddNeuroMed study. *Ann N Y Acad Sci* [Internet]. 2009  
1315 Oct;1180:47–55. Available from: <http://dx.doi.org/10.1111/j.1749-6632.2009.05063.x>
- 1316 72. Allen GI, Amoroso N, Anghel C, Balagurusamy V, Bare CJ, Beaton D, et al. Crowdsourced  
1317 estimation of cognitive decline and resilience in Alzheimer’s disease. *Alzheimers Dement*  
1318 [Internet]. 2016 Jun [cited 2016 Aug 6];12(6):645–53. Available from:  
1319 <http://dx.doi.org/10.1016/j.jalz.2016.02.006>
- 1320 73. Van Essen DC, Drury HA, Dickson J, Harwell J, Hanlon D, Anderson CH. An integrated software  
1321 suite for surface-based analyses of cerebral cortex. *J Am Med Inform Assoc* [Internet]. 2001  
1322 Sep;8(5):443–59. Available from: <http://www.ncbi.nlm.nih.gov/pubmed/11522765>
- 1323 74. Fischl B, Salat DH, Busa E, Albert M, Dieterich M, Haselgrove C, et al. Whole brain segmentation:  
1324 automated labeling of neuroanatomical structures in the human brain. *Neuron* [Internet]. 2002 Jan  
1325 31;33(3):341–55. Available from: <http://www.ncbi.nlm.nih.gov/pubmed/11832223>
- 1326 75. Tustison NJ, Cook PA, Klein A, Song G, Das SR, Duda JT, et al. Large-scale evaluation of ANTs  
1327 and FreeSurfer cortical thickness measurements. *Neuroimage* [Internet]. 2014 Oct 1 [cited 2016  
1328 Aug 6];99:166–79. Available from: <http://dx.doi.org/10.1016/j.neuroimage.2014.05.044>
- 1329 76. Avants BB, Tustison NJ, Wu J, Cook PA, Gee JC. An open source multivariate framework for n-  
1330 tissue segmentation with evaluation on public data. *Neuroinformatics* [Internet]. 2011 Dec [cited  
1331 2016 Aug 6];9(4):381–400. Available from: <http://dx.doi.org/10.1007/s12021-011-9109-y>
- 1332 77. Klauschen F, Goldman A, Barra V, Meyer-Lindenberg A, Lundervold A. Evaluation of automated  
1333 brain MR image segmentation and volumetry methods. *Hum Brain Mapp* [Internet]. 2009

- 1334 Apr;30(4):1310–27. Available from: <http://dx.doi.org/10.1002/hbm.20599>
- 1335 78. Winkler AM, Kochunov P, Blangero J, Almasy L, Zilles K, Fox PT, et al. Cortical thickness or  
1336 grey matter volume? The importance of selecting the phenotype for imaging genetics studies.  
1337 Neuroimage [Internet]. 2010 Nov 15 [cited 2016 Aug 6];53(3):1135–46. Available from:  
1338 <http://dx.doi.org/10.1016/j.neuroimage.2009.12.028>
- 1339 79. Lorio S, Kherif F, Ruef A, Melie-Garcia L, Frackowiak R, Ashburner J, et al. Neurobiological  
1340 origin of spurious brain morphological changes: A quantitative MRI study: Computational  
1341 Anatomy Studies of the Brain. Hum Brain Mapp [Internet]. 2016 May [cited 2016 Aug  
1342 6];37(5):1801–15. Available from: <http://dx.doi.org/10.1002/hbm.23137>
- 1343 80. Fischl B, Dale AM. Measuring the thickness of the human cerebral cortex from magnetic resonance  
1344 images. Proceedings of the National Academy of Sciences [Internet]. 2000 Sep 26 [cited 2016 Aug  
1345 6];97(20):11050–5. Available from: <http://dx.doi.org/10.1073/pnas.200033797>
- 1346 81. Han X, Jovicich J, Salat D, van der Kouwe A, Quinn B, Czanner S, et al. Reliability of MRI-  
1347 derived measurements of human cerebral cortical thickness: the effects of field strength, scanner  
1348 upgrade and manufacturer. Neuroimage [Internet]. 2006 Aug 1 [cited 2016 Aug 6];32(1):180–94.  
1349 Available from: <http://dx.doi.org/10.1016/j.neuroimage.2006.02.051>
- 1350 82. Dahnke R, Yotter RA, Gaser C. Cortical thickness and central surface estimation. Neuroimage  
1351 [Internet]. 2013 Jan 15 [cited 2016 Aug 6];65:336–48. Available from:  
1352 <http://dx.doi.org/10.1016/j.neuroimage.2012.09.050>
- 1353 83. Lüsebrink F, Wollrab A, Speck O. Cortical thickness determination of the human brain using high  
1354 resolution 3T and 7T MRI data. Neuroimage [Internet]. 2013 Apr 15 [cited 2016 Aug 6];70:122–  
1355 31. Available from: <http://dx.doi.org/10.1016/j.neuroimage.2012.12.016>
- 1356 84. Salat DH, Buckner RL, Snyder AZ, Greve DN, Desikan RSR, Busa E, et al. Thinning of the  
1357 cerebral cortex in aging. Cereb Cortex [Internet]. 2004 Jul [cited 2016 Aug 6];14(7):721–30.  
1358 Available from: <http://dx.doi.org/10.1093/cercor/bhh032>
- 1359 85. Fjell AM, Westlye LT, Amlien I, Espeseth T, Reinvang I, Raz N, et al. High consistency of  
1360 regional cortical thinning in aging across multiple samples. Cereb Cortex [Internet]. 2009 Sep  
1361 [cited 2016 Aug 6];19(9):2001–12. Available from: <http://dx.doi.org/10.1093/cercor/bhn232>
- 1362 86. Winkler AM, Sabuncu MR, Yeo BTT, Fischl B, Greve DN, Kochunov P, et al. Measuring and  
1363 comparing brain cortical surface area and other areal quantities. Neuroimage [Internet]. 2012 Jul 16  
1364 [cited 2016 Aug 6];61(4):1428–43. Available from:  
1365 <http://dx.doi.org/10.1016/j.neuroimage.2012.03.026>
- 1366 87. Deppe M, Marinell J, Krämer J, Duning T, Ruck T, Simon OJ, et al. Increased cortical curvature  
1367 reflects white matter atrophy in individual patients with early multiple sclerosis. Neuroimage Clin  
1368 [Internet]. 2014 Mar 3 [cited 2016 Aug 6];6:475–87. Available from:  
1369 <http://dx.doi.org/10.1016/j.nicl.2014.02.012>
- 1370 88. King JB, Lopez-Larson MP, Yurgelun-Todd DA. Mean cortical curvature reflects cytoarchitecture  
1371 restructuring in mild traumatic brain injury. Neuroimage Clin [Internet]. 2016 Jan 6 [cited 2016  
1372 Aug 6];11:81–9. Available from: <http://dx.doi.org/10.1016/j.nicl.2016.01.003>

- 1373 89. Ronan L, Pienaar R, Williams G, Bullmore E, Crow TJ, Roberts N, et al. Intrinsic curvature: a  
1374 marker of millimeter-scale tangential cortico-cortical connectivity? *Int J Neural Syst* [Internet].  
1375 2011 Oct [cited 2016 Aug 6];21(5):351–66. Available from:  
1376 <http://dx.doi.org/10.1142/S0129065711002948>
- 1377 90. Ronan L, Voets N, Rua C, Alexander-Bloch A, Hough M, Mackay C, et al. Differential tangential  
1378 expansion as a mechanism for cortical gyrification. *Cereb Cortex* [Internet]. 2014 Aug [cited 2016  
1379 Aug 6];24(8):2219–28. Available from: <http://dx.doi.org/10.1093/cercor/bht082>
- 1380 91. Rettmann ME, Han X, Xu C, Prince JL. Automated sulcal segmentation using watersheds on the  
1381 cortical surface. *Neuroimage* [Internet]. 2002 Feb [cited 2016 Aug 6];15(2):329–44. Available  
1382 from: <http://dx.doi.org/10.1006/nimg.2001.0975>
- 1383 92. Lohmann G, von Cramon DY. Automatic labelling of the human cortical surface using sulcal  
1384 basins. *Med Image Anal* [Internet]. 2000 Sep;4(3):179–88. Available from:  
1385 <http://www.ncbi.nlm.nih.gov/pubmed/11145307>
- 1386 93. Kao C-Y, Hofer M, Sapiro G, Stem J, Rehm K, Rottenberg DA. A geometric method for automatic  
1387 extraction of sulcal fundi. *IEEE Trans Med Imaging* [Internet]. 2007 Apr;26(4):530–40. Available  
1388 from: <http://dx.doi.org/10.1109/TMI.2006.886810>
- 1389 94. Li G, Liu T, Nie J, Guo L, Wong STC. A novel method for cortical sulcal fundi extraction. *Med*  
1390 *Image Comput Comput Assist Interv* [Internet]. 2008;11(Pt 1):270–8. Available from:  
1391 <http://www.ncbi.nlm.nih.gov/pubmed/18979757>
- 1392 95. Le Troter A, Auzias G, Coulon O. Automatic sulcal line extraction on cortical surfaces using  
1393 geodesic path density maps. *Neuroimage* [Internet]. 2012 Jul 16;61(4):941–9. Available from:  
1394 <http://dx.doi.org/10.1016/j.neuroimage.2012.04.021>
- 1395 96. Im K, Jo HJ, Mangin J-F, Evans AC, Kim SI, Lee J-M. Spatial distribution of deep sulcal  
1396 landmarks and hemispherical asymmetry on the cortical surface. *Cereb Cortex* [Internet]. 2010 Mar  
1397 [cited 2016 Aug 6];20(3):602–11. Available from: <http://dx.doi.org/10.1093/cercor/bhp127>
- 1398 97. Im K, Pienaar R, Lee J-M, Seong J-K, Choi YY, Lee KH, et al. Quantitative comparison and  
1399 analysis of sulcal patterns using sulcal graph matching: a twin study. *Neuroimage* [Internet]. 2011  
1400 Aug 1 [cited 2016 Aug 6];57(3):1077–86. Available from:  
1401 <http://dx.doi.org/10.1016/j.neuroimage.2011.04.062>
- 1402 98. Coleman RG, Sharp KA. Travel depth, a new shape descriptor for macromolecules: application to  
1403 ligand binding. *J Mol Biol* [Internet]. 2006 Sep 22 [cited 2016 Aug 6];362(3):441–58. Available  
1404 from: <http://dx.doi.org/10.1016/j.jmb.2006.07.022>
- 1405 99. Giard J, Alface PR, Gala J-L, Macq B. Fast surface-based travel depth estimation algorithm for  
1406 macromolecule surface shape description. *IEEE/ACM Trans Comput Biol Bioinform* [Internet].  
1407 2011 Jan [cited 2016 Aug 6];8(1):59–68. Available from: <http://dx.doi.org/10.1109/TCBB.2009.53>
- 1408 100. Yun HJ, Im K, Jin-Ju Yang, Yoon U, Lee J-M. Automated sulcal depth measurement on cortical  
1409 surface reflecting geometrical properties of sulci. Draganski B, editor. *PLoS One* [Internet]. 2013  
1410 Feb 13 [cited 2016 Aug 6];8(2):e55977. Available from:  
1411 <http://dx.doi.org/10.1371/journal.pone.0055977>

- 1412 101. Boucher M, Whitesides S, Evans A. Depth potential function for folding pattern representation,  
1413 registration and analysis. *Med Image Anal* [Internet]. 2009 Apr [cited 2016 Aug 6];13(2):203–14.  
1414 Available from: <http://dx.doi.org/10.1016/j.media.2008.09.001>
- 1415 102. Bao F, Lee N, Hame Y, Im K, Riviera D, Li G, et al. Automated extraction of nested sulcal  
1416 features from human brain MRI data. In: 17th annual meeting for the Organization of Human Brain  
1417 Mapping [Internet]. 2011. Available from:  
1418 [https://github.com/binarybottle/nestedsulcusfeatures\\_HBM2011](https://github.com/binarybottle/nestedsulcusfeatures_HBM2011)
- 1419 103. Lee N, Klein A. A graph-based database of hierarchical brain features. In: *Frontiers in*  
1420 *Neuroinformatics* [Internet]. 2011 [cited 2016 Aug 6]. Available from:  
1421 [http://www.frontiersin.org/10.3389/conf.fninf.2011.08.00139/event\\_abstract](http://www.frontiersin.org/10.3389/conf.fninf.2011.08.00139/event_abstract)
- 1422 104. Reuter M, Wolter F-E, Peinecke N. Laplace–Beltrami spectra as “Shape-DNA” of surfaces and  
1423 solids. *Comput Aided Des Appl* [Internet]. 2006/4 [cited 2016 Aug 6];38(4):342–66. Available  
1424 from: <http://www.sciencedirect.com/science/article/pii/S0010448505001867>
- 1425 105. Reuter M, Wolter F-E, Shenton M, Niethammer M. Laplace–Beltrami eigenvalues and  
1426 topological features of eigenfunctions for statistical shape analysis. *Comput Aided Des Appl*  
1427 [Internet]. 2009 Oct [cited 2016 Aug 6];41(10):739–55. Available from:  
1428 <http://www.sciencedirect.com/science/article/pii/S0010448509000463>
- 1429 106. Reuter M, Schmansky NJ, Rosas HD, Fischl B. Within-subject template estimation for unbiased  
1430 longitudinal image analysis. *Neuroimage* [Internet]. 2012 Jul 16 [cited 2016 Aug 6];61(4):1402–18.  
1431 Available from: <http://dx.doi.org/10.1016/j.neuroimage.2012.02.084>
- 1432 107. Konukoglu E, Glocker B, Criminisi A, Pohl KM. WESD--Weighted Spectral Distance for  
1433 measuring shape dissimilarity. *IEEE Trans Pattern Anal Mach Intell* [Internet]. 2013 Sep [cited  
1434 2016 Aug 6];35(9):2284–97. Available from: <http://dx.doi.org/10.1109/TPAMI.2012.275>
- 1435 108. Celebi ME, Aslandogan YA. A comparative study of three moment-based shape descriptors. In:  
1436 *International Conference on Information Technology: Coding and Computing (ITCC'05) - Volume*  
1437 *II* [Internet]. IEEE; 2005 [cited 2016 Aug 6]. p. 788–93 Vol. 1. Available from:  
1438 <http://dx.doi.org/10.1109/ITCC.2005.3>
- 1439 109. Mangin J-F, Poupon F, Duchesnay E, Rivière D, Cachia A, Collins DL, et al. Brain  
1440 morphometry using 3D moment invariants. *Med Image Anal* [Internet]. 2004 Sep [cited 2016 Aug  
1441 6];8(3):187–96. Available from: <http://dx.doi.org/10.1016/j.media.2004.06.016>
- 1442 110. Novotni M, Klein R. Shape retrieval using 3D Zernike descriptors. *Comput Aided Des Appl*  
1443 [Internet]. 2004 Sep 15 [cited 2016 Aug 6];36(11):1047–62. Available from:  
1444 <http://www.sciencedirect.com/science/article/pii/S0010448504000077>
- 1445 111. Pozo JM, Villa-Uriol M-C, Frangi AF. Efficient 3D geometric and Zernike moments  
1446 computation from unstructured surface meshes. *IEEE Trans Pattern Anal Mach Intell* [Internet].  
1447 2011 Mar;33(3):471–84. Available from: <http://dx.doi.org/10.1109/TPAMI.2010.139>
- 1448 112. Mazziotta J, Toga A, Evans A, Fox P, Lancaster J, Zilles K, et al. A probabilistic atlas and  
1449 reference system for the human brain: International Consortium for Brain Mapping (ICBM). *Philos*  
1450 *Trans R Soc Lond B Biol Sci* [Internet]. 2001 Aug 29 [cited 2016 Aug 6];356(1412):1293–322.  
1451 Available from: <http://dx.doi.org/10.1098/rstb.2001.0915>

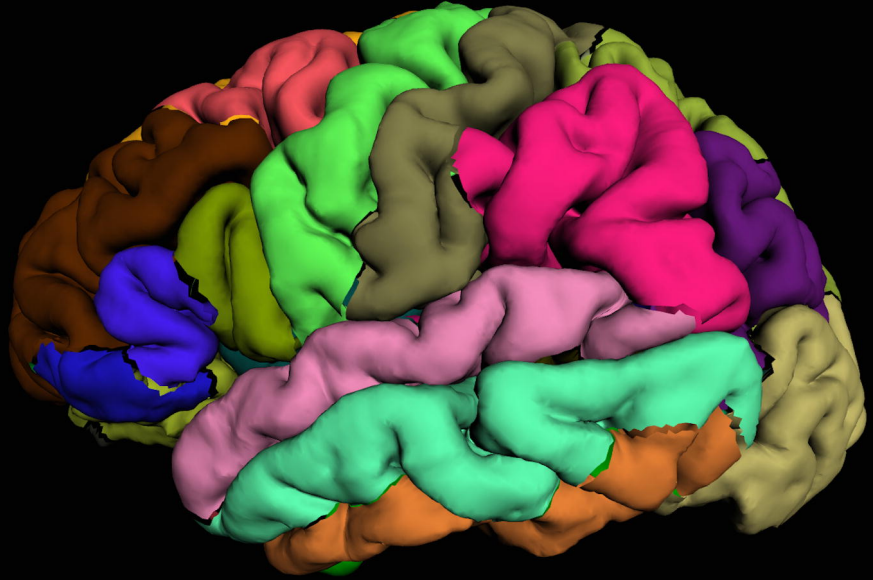
- 1452 113. Rosas HD, Liu AK, Hersch S, Glessner M, Ferrante RJ, Salat DH, et al. Regional and  
1453 progressive thinning of the cortical ribbon in Huntington's disease. *Neurology* [Internet]. 2002 Mar  
1454 12 [cited 2016 Aug 6];58(5):695–701. Available from:  
1455 <http://www.ncbi.nlm.nih.gov/pubmed/11889230>
- 1456 114. Kabani N, Le Goualher G, MacDonald D, Evans AC. Measurement of Cortical Thickness Using  
1457 an Automated 3-D Algorithm: A Validation Study. *Neuroimage* [Internet]. 02/2001 [cited 2016 Jun  
1458 27];13(2):375–80. Available from: <http://linkinghub.elsevier.com/retrieve/pii/S1053811900906529>
- 1459 115. Li G, Guo L, Nie J, Liu T. An automated pipeline for cortical sulcal fundi extraction. *Med Image*  
1460 *Anal* [Internet]. 2010 Jun [cited 2016 Aug 6];14(3):343–59. Available from:  
1461 <http://dx.doi.org/10.1016/j.media.2010.01.005>
- 1462 116. Jovicich J, Marizzoni M, Sala-Llonch R, Bosch B, Bartrés-Faz D, Arnold J, et al. Brain  
1463 morphometry reproducibility in multi-center 3T MRI studies: a comparison of cross-sectional and  
1464 longitudinal segmentations. *Neuroimage* [Internet]. 2013 Dec;83:472–84. Available from:  
1465 <http://dx.doi.org/10.1016/j.neuroimage.2013.05.007>
- 1466 117. Klein A, Chaibub Neto E, Giard J, Bao F, Hame Y, Reuter M, et al. Shape analysis of 101  
1467 healthy human brains. In: 20th annual meeting for the Organization of Human Brain Mapping  
1468 [Internet]. 2014. Available from:  
1469 <https://mfr.osf.io/render?url=https://osf.io/w2vda/?action=download%26mode=render>
- 1470 118. Klein A, Chaibub Neto E, Ghosh S, ADNI. Detailed shape analysis of healthy brains and brains  
1471 with Alzheimer's disease. In: 21st annual meeting for the Organization of Human Brain Mapping  
1472 [Internet]. 2015. Available from:  
1473 <https://mfr.osf.io/render?url=https://osf.io/xfts3/?action=download%26mode=render>
- 1474 119. Zuo X-N, Anderson JS, Bellec P, Birn RM, Biswal BB, Blautzik J, et al. An open science  
1475 resource for establishing reliability and reproducibility in functional connectomics. *Sci Data*  
1476 [Internet]. 2014 Dec 9 [cited 2016 Aug 6];1:140049. Available from:  
1477 <http://dx.doi.org/10.1038/sdata.2014.49>
- 1478 120. Maclaren J, Han Z, Vos SB, Fischbein N, Bammer R. Reliability of brain volume measurements:  
1479 a test-retest dataset. *Scientific Data* [Internet]. 2014 Oct 14 [cited 2016 Aug 6];1:140037. Available  
1480 from: <http://dx.doi.org/10.1038/sdata.2014.37>
- 1481 121. Huang L, Huang T, Zhen Z, Liu J. A test-retest dataset for assessing long-term reliability of brain  
1482 morphology and resting-state brain activity. *Sci Data* [Internet]. 2016 Mar 15 [cited 2016 Aug  
1483 6];3:160016. Available from: <http://dx.doi.org/10.1038/sdata.2016.16>
- 1484 122. Holmes AJ, Hollinshead MO, O'Keefe TM, Petrov VI, Fariello GR, Wald LL, et al. Brain  
1485 Genomics Superstruct Project initial data release with structural, functional, and behavioral  
1486 measures. *Sci Data* [Internet]. 2015 Jul 7 [cited 2016 Aug 6];2:150031. Available from:  
1487 <http://dx.doi.org/10.1038/sdata.2015.31>
- 1488 123. Van Essen DC, Smith SM, Barch DM, Behrens TEJ, Yacoub E, Ugurbil K, et al. The WU-Minn  
1489 Human Connectome Project: an overview. *Neuroimage* [Internet]. 2013 Oct 15 [cited 2016 Aug  
1490 6];80:62–79. Available from: <http://dx.doi.org/10.1016/j.neuroimage.2013.05.041>
- 1491 124. Gorgolewski KJ, Mendes N, Wilfling D, Wladimirow E, Gauthier CJ, Bonnen T, et al. A high

- 1492 resolution 7-Tesla resting-state fMRI test-retest dataset with cognitive and physiological measures.  
1493 Sci Data [Internet]. 2015 Jan 20 [cited 2016 Aug 6];2:140054. Available from:  
1494 <http://dx.doi.org/10.1038/sdata.2014.54>
- 1495 125. Auzias G, Brun L, Deruelle C, Coulon O. Benchmark data for sulcal pits extraction algorithms.  
1496 Data Brief [Internet]. 2015 Dec [cited 2016 Aug 6];5:595–8. Available from:  
1497 <http://dx.doi.org/10.1016/j.dib.2015.10.004>
- 1498 126. Huo Y, Plassard AJ, Carass A, Resnick SM, Pham DL, Prince JL, et al. Consistent cortical  
1499 reconstruction and multi-atlas brain segmentation. Neuroimage [Internet]. 2016 Sep;138:197–210.  
1500 Available from: <http://dx.doi.org/10.1016/j.neuroimage.2016.05.030>
- 1501 127. Schmidhuber J. Deep learning in neural networks: an overview. Neural Netw [Internet]. 2015 Jan  
1502 [cited 2016 Aug 6];61:85–117. Available from: <http://dx.doi.org/10.1016/j.neunet.2014.09.003>
- 1503 128. Lee N, Laine AF, Klein A. Towards a deep learning approach to brain parcellation. In: 2011  
1504 IEEE International Symposium on Biomedical Imaging: From Nano to Macro [Internet]. IEEE;  
1505 2011 [cited 2016 Aug 6]. p. 321–4. Available from: <http://dx.doi.org/10.1109/ISBI.2011.5872414>
- 1506

# ROYGBIV

Shift+click on a label to see stats

Selected Label:



# ROYGBIV

Shift+click on a label to see stats

Selected Label: 1031

## Shape distributions

